

ALMA MATER STUDIORUM
UNIVERSITÀ DEGLI STUDI DI BOLOGNA

Science's school
Department of Physics and Astronomy - DIFA
Second cycle degree/two year master in Astrophysics and Cosmology

Master's degree thesis

**Assessing the turbulent pressure in galaxy
clusters**

Candidate:
Matteo Angelinelli

Supervisor:
Dr. Franco Vazza

Session II
Academic year 2017-2018

Abstract

The amount of turbulent pressure support residual gas motions at the periphery of galaxy clusters is not well known. Direct (e.g. X-ray Doppler shift) or indirect (e.g. X-ray brightness fluctuations, radio halo emission or Faraday Rotation) proxies of turbulence are not effective at the periphery of galaxy clusters. On the other hand, the presence a significant non-thermal pressure support in galaxy clusters on large scales is suggested by the mass modelling of combined X-ray and Sunyaev Zel'dovich observations. Cosmological simulations may help estimating this budget, yet in the literature a still wide range of estimates (from a few percent to half of the gas pressure) is typically found, depending on the specific procedure to disentangle bulk from random turbulent motions. In this Thesis, we tested different operative choices for the filtering of laminar and bulk gas motions from simulated datasets, and we produced new analysis of turbulence in galaxy clusters with a large catalog of cluster simulations using the adaptive mesh refinement code *ENZO*.

Several methods have been produced in the literature to extract turbulence in the simulated intracluster medium, and in this Thesis we have explored the application of different filtering scales for the velocity field, exploring the range from 60 to 600 kpc, in order to robustly tell laminar from turbulent motions apart. Moreover, since shocks can introduce spurious terms in the non-thermal pressure, so to avoid these terms, we apply a tailored shocks finding algorithm to minimise their contribution to the estimated turbulent budget.

We mostly focused on the ratio of non-thermal pressure versus total pressure (thermal and non-thermal pressure) and its dependence with the distance from the center of the cluster, finding that the radial behavior is well described by a simple polynomial formula. The typical non-thermal pressure support we measured in the center of cluster is $\sim 0.1\%-5\%$ (depending on the filtering scale), while this reaches $\sim 0.5\%-10\%$ within the same range of spatial scales for the filtering. We have also compared our results with recent numerical and observational literature. In particular, from the comparison with [Nelson et al. \(2014\)](#), we found that the different definition of turbulent velocity generates very different amount of turbulent support. As we also discussed in a related paper ([Vazza et al., 2018](#), in press) previous

techniques overestimate the turbulent pressure by a factor 2 or 3, while from the fitting procedure which we used, we found that our fitting formula is more statistically significant than the Nelson's model.

In the paper by [Eckert et al. \(2018\)](#) estimates of the non-thermal to total pressure for a sample of 13 galaxy clusters observed with XMM-Newton have been reported, at R_{500} and R_{200} . Our results allow us to compare with these latest estimates, and assess which turbulent spatial scale best reproduces the observed trends.

We have also studied the relation between the ratio of non-thermal pressure versus total pressure at R_{200} and smoothing scale, in order to test whether the "standard" relation between rms velocity and turbulent scale (e.g. $\sigma^2 \propto L^{\frac{2}{3}}$) based on Kolmogorov theory also holds for our data. We found an overall close match to the Kolmogorov model, with differences related to the fact that the power spectra of the velocity field in simulated galaxy cluster are typically steeper than $\frac{5}{3}$, because of the stratified cluster atmosphere.

We also studied the relations between non-thermal support and cluster's mass or dynamical state. In particular, these study have shown that there are not any strong correlations between these quantities. We conclude that our no complete mass selection of the sample affect the study of any possible correlation. However, we found that the X-ray morphological parameter 'c' and 'w' shown different behavior. In particular, the first is a weak indicator of turbulence in the innermost region of the cluster, but it could not be used as an indicator of turbulent motions in the outskirts. Indeed, 'w' parameter is a weak indicator of turbulent motions at most radii.

Some of the key results of this Thesis are already part of a work which is submitted ([Vazza et al., 2018](#), in press) and will be further documented in a dedicated scientific paper ([Angelinelli et al.](#), in prep.).

Sommario

La quantità di pressione associata ai moti residui turbolenti del gas nelle regioni esterne degli ammassi di galassie non è ben nota. Osservazioni dirette (e.g. Doppler shift dei fotoni X) o indirette (e.g. fluttuazioni della brillantezza X, emissione degli aloni radio o effetti della rotazione di Faraday) non riescono ancora a caratterizzare la pressione turbolenta nelle zone più periferiche degli ammassi. Da modelli combinati di osservazioni in banda X e Sunyaev Zel'dovich, dai quali è possibile ricavare la massa degli ammassi, emerge la necessità di una componente non termica alla pressione del gas. Le simulazioni cosmologiche possono essere usate per determinare l'intervallo in cui questo contributo non termico (da pochi per cento fino a circa il 50% della pressione totale) può variare, ma tale intervallo è fortemente dipendente dalle procedure con le quali si filtrano i moti turbolenti e i moti laminari. In questa tesi, abbiamo testato diverse scelte operative di questi filtri con un campione di ammassi simulati e generati usando il codice con griglia adattiva *ENZO*.

In letteratura sono presenti diversi metodi di estrazione dei moti turbolenti dal mezzo intracluster simulato, e in questa tesi abbiamo studiato gli effetti di un filtraggio a diverse scale del campo di velocità, con filtri da 60 a 600 kpc, in modo da avere una definizione robusta di moti turbolenti e moti laminari. Inoltre, anche gli shock possono introdurre nel mezzo una componente di pressione non termica e quindi per escludere termini spuri alla pressione turbolenta, abbiamo applicato un algoritmo per l'identificazione e la rimozione dei contributi aggiuntivi degli shock all'energia cinetica turbolenta.

In particolare abbiamo incentrato il nostro studio sul rapporto pressione non termica su pressione totale (la somma di pressione termica e non termica), e studiandone l'andamento radiale. Abbiamo trovato che questo è ben descritto da una semplice funzione polinomiale. I valori tipici del contributo non termico nel centro degli ammassi si attestano tra $\sim 0.1\%$ e 5% (con una dipendenza dalla scala di filtraggio scelta), mentre raggiungono $\sim 0.5\%$ - 10% nelle zone più esterne (con la stessa dipendenza dalla scala di filtraggio). Abbiamo inoltre confrontato i nostri risultati con lavori presenti in letteratura, sia con risultati derivanti da osservazioni

che da simulazioni. In particolare, dal confronto con [Nelson et al. \(2014\)](#) abbiamo notato che la diversa definizione di moti turbolenti genera risultati molto differenti nel contributo non termico alla pressione. Abbiamo anche discusso nell'articolo [Vazza et al. \(2018, in press\)](#) come le tecniche precedentemente usate sovrastimino la pressione turbolenta di un fattore 2 o 3, mentre dal confronto statistico tra il nostro modello e quello di Nelson applicato al nostro campione, è emerso che il modello da noi proposto è statisticamente più significativo.

Nell'articolo di [Eckert et al. \(2018\)](#) viene stimato il rapporto tra la pressione non termica e quella totale a R_{500} e R_{200} per un campione di 13 ammassi osservati con XMM-Newton. Abbiamo usato questi risultati per determinare quale scala di filtraggio da noi usata meglio riproduce i dati osservati.

Abbiamo anche studiato la relazione tra la pressione non termica e totale calcolata a R_{200} e la scala di filtraggio, per verificare se la relazione 'standard' tra dispersione di velocità e scala turbolenta (e.g. $\sigma^2 \propto L^{\frac{2}{3}}$) derivata dalla teoria di Kolmogorov è applicabile ai nostri dati. Abbiamo verificato che le previsioni attese dalla teoria sono state rispettate, trovando tuttavia come lo spettro di potenza del campo di velocità negli ammassi di galassie simulati sia più ripido del valore $\frac{5}{3}$ previsto dalla teoria di Kolmogorov, a causa della stratificazione in densità del mezzo intracluster.

Abbiamo quindi studiato le relazioni tra supporto non termico alla pressione e massa o stato dinamico degli ammassi. In particolare, abbiamo trovato che non ci sono forti correlazioni tra le quantità studiate. Abbiamo concluso che il fatto di non avere un campione completo in massa rende difficile studiare a fondo queste dipendenze. Abbiamo però potuto esplorare la dipendenza della turbolenza da due parametri morfologici usati nelle osservazioni X, i parametri 'c' e 'w'. Questi parametri mostrano un comportamento nettamente diverso tra loro. Il parametro 'c' è un indicatore debole di turbolenza nelle zone più centrali degli ammassi, ma non può essere utilizzato come estimatore di pressione turbolenta nelle regioni esterne. Il parametro 'w', invece, è un indicatore debole di turbolenza in tutta l'estensione dell'ammasso.

Alcuni dei risultati trovati in questa tesi sono già parte di un articolo che è stato sottomesso ([Vazza et al., 2018, in press](#)), ed altri saranno parte di un articolo scientifico interamente dedicato a tutti gli argomenti trattati in questa tesi ([Angelinelli et al., in prep.](#)).

Contents

| | | |
|----------|---|-----------|
| 1 | Introduction | 1 |
| 1.1 | Clusters of galaxies in a cosmological context | 1 |
| 1.2 | Observational features | 2 |
| 1.3 | ICM: Intra Cluster Medium | 6 |
| 1.3.1 | Virial Theorem | 6 |
| 1.3.2 | Self-similar scaling relations | 8 |
| 1.3.3 | Hydrostatic model | 11 |
| 2 | Turbulence | 13 |
| 2.1 | Theoretical bases | 13 |
| 2.2 | Turbulence in galaxy clusters | 18 |
| 2.2.1 | Ram Pressure Stripping | 20 |
| 2.2.2 | Injection of turbulence by shocks | 21 |
| 2.2.3 | Injection by AGN | 21 |
| 2.3 | Simulated turbulence in the ICM | 22 |
| 2.4 | Observational indications of turbulence in the ICM | 24 |
| 3 | Numerical Analysis | 27 |
| 3.1 | Effects of the filtering scale on turbulence | 27 |
| 3.2 | Limiting the spurious contribution from shocks to the turbulent budget | 29 |
| 3.2.1 | Shock Finder | 31 |
| 4 | Results and analysis | 35 |
| 4.1 | Cluster catalog | 35 |
| 4.2 | Complete sample analysis | 39 |
| 4.3 | Relation between the filtering scale of turbulence and the non-thermal pressure support | 43 |
| 4.4 | Sub-samples analysis | 45 |
| 4.4.1 | Mass division | 46 |

CONTENTS

| | | |
|----------|---|-----------|
| 4.4.2 | Dynamic state division | 48 |
| 4.5 | Comparison with recent literature | 55 |
| 5 | Conclusions and future perspectives | 59 |
| A | Numerical algorithm | 65 |
| B | Fitting parameters for sub-samples | 67 |

Chapter 1

Introduction

In this first chapter we analyse the role of galaxy clusters in cosmological context and we make a brief introduction of the basic mechanisms that they are typical of large scale structures formation.

1.1 Clusters of galaxies in a cosmological context

In this section we describe the modern cosmological scenario and the importance of galaxy clusters in cosmology. We follow the review by [Planelles et al. \(2015\)](#) and the references therein.

The current hierarchical paradigm of structure formation is set within the spatially flat Λ -Cold Dark Matter model (Λ CDM) with a cosmological constant. In this paradigm the Universe, whose age is estimated to be 13.8 Gyr, is composed of dark energy ($\Omega_\Lambda \approx 0.7$), dark matter ($\Omega_{\text{DM}} \approx 0.25$) and baryonic matter ($\Omega_b \approx 0.05$), with a Hubble constant given by $H_0 \approx 67$ [$\text{km s}^{-1} \text{Mpc}^{-1}$].

In the hierarchical paradigm of structure formation, the massive objects like galaxies and galaxy clusters are formed through accretion and mergers. The first objects which are formed in early Universe, from redshift 30 to 10, are believed to be massive isolated stars of about $\sim 100\text{-}300 M_\odot$. The formation sites of these stars are mini halos of dark matter with masses in a range between $\sim 10^5\text{-}10^8 M_\odot$.

Galaxy clusters, the largest and most massive objects in our Universe, formed from the smaller units into a sequence of mergers. A simplistic and commonly accepted model is the self-similar model by [Kaiser \(1986\)](#) which is based on Einstein-de Sitter background cosmology and a power law shape for the power spectrum of primordial density fluctuations. As result of this model we obtain the self-similar relations which describe the intra-cluster medium and which will be investigated in section 1.3.2. However, the full description of cluster formation requires detailed modeling of the nonlinear processes of collapse and the dissipative physics

of baryons.

The study of galaxy clusters is fundamental to understand some cosmological issues and to compute the values of some cosmological parameters in a way complementary to other astrophysical probes (e.g. high redshift supernovae and cosmic microwave background). In particular, the abundance and spatial distribution of clusters are useful to have information about the background cosmology, gravity law, and initial conditions, while the nearly closed-box nature of cluster gravitational potentials makes it possible to study the processes operating during galaxy formation and their effects on the surrounding intergalactic medium.

The fundamental role of clusters in the cosmological context is also highlighted by future space missions. As described in [Sartoris et al. \(2016\)](#) the space mission Euclid, whose launch is scheduled for 2021, will enable to identify photometrically more than one million clusters, of which about half a million of which redshift higher than 1 and ~ 2000 with redshift greater than 2. The fundamental quantity use as cosmological probes is cluster mass. Using the effects of gravitational lensing, the number counts and the total luminosity of the galaxies in the clusters and their velocity distribution, it will be possible to calibrate the relations mass-dependent with excellent precision ($\sim 10\%$) down to redshift ~ 1.5 . The Euclid mission therefore has the power to determine the fundamental cosmological constants with excellent precision and therefore to define which model best describes our Universe.

1.2 Observational features

Now we summarize the principal observational features obtained from optical, X-ray and radio band observations and Sunyaev-Zel'dovich effect (SZ effect).

- **Optical band:** in this band the radiation is dominated by the Black Body emission of the stars within galaxies. This emission is described by Plank's law. In particular, it is possible to study the radial velocity of the galaxies and the interactions between galaxies (e.g. ram pressure stripping, high speed galaxy encounters, tidal stripping and etc.). Other possible studies are the galaxy morphological distribution (e.g. how many early type or late type galaxies are confined in the cluster) and the evolution of the galaxies in a high density environment. A further phenomenon that can be studied in this band is gravitational lensing. Photons from a source placed beyond the cluster are deflected by the cluster's gravitational field. The cluster therefore acts as a gravitational lens and through the study of lensing maps it is possible to determine the mass of the cluster with considerable precision;

- **X-ray band:** in this band there are mainly two emission mechanisms. The first is the thermal bremsstrahlung, whose X brightness depends on the temperature and density of the gas. The second is the lines emission of metals, which emit at specific energies (e.g. the FeXV fluorescence line $K\alpha$ at 6.4 keV). From the observations in this band it is possible to derive density and temperature profiles of the ICM gas and to study the broadening of the metal lines, which give us information on the velocity fields of the gas. Thanks to the broadening of the metal lines, it is in principle possible to study the turbulence in the ICM medium observably, but a high spectral resolution is required, which is presently difficult to achieve in this band. From the observation of the density, temperature and entropy profiles, it has been possible to infer the 'Cooling flow problem' and the distinction between cool-core clusters (CC) and no cool-core ones (NCC). CC clusters have density peak in the central areas. Their profile is well described by the double β -model, an empiric fit which, however, does not explain the origin of this peak. Furthermore, these clusters have a drop in the temperature profile. From the observed density peak, CC clusters are thought to be relaxed systems that do not undergo major mergers from some Gyr. The NCC clusters are instead associated with recent merger phenomena and are believed to be more turbulent systems. The cooling flow problem stems from the fact that for too large gas density, the gas in the center of many galaxy clusters should have radiated away most of its energy in a Hubble time. This motivated the idea of feedback mechanisms. In fact, it is expected from the theory that in the center of the cluster a considerable quantity of gas is observed at temperatures below 10^4 K, but from the observations, it has never been detected. To date, the main candidate is AGN feedback, a self-regulated mechanism which alternates cooling and heating phases (see [Brighenti & Mathews, 2002](#); [Gaspari et al., 2011, 2018](#), for details). There are some morphological parameters in this band (e.g. 'w' centroid shift and 'c' concentration which will also be used in this thesis in section 4.4.2), which are used to distinguish relaxed and perturbed clusters. A more detailed overview of the properties of the ICM in galaxy clusters is given in the next section;
- **Radio band:** in this band the observed radiation is dominated mainly by synchrotron radiation. Synchrotron emission occurs when a relativistic electron coils around the lines of a magnetic field. Assuming a distribution of the energy for the individual electrons proportional to $E^{-\delta}$, where δ is derived from the energy spectrum of cosmic rays, the total synchrotron emission spectrum is described by a power law. In galaxy clusters we can observe radio emission typically from three classes of objects: relics, halos and mini-halos.

The first are located in the periphery of the clusters, and generally elongated shape in a direction perpendicular to the radial direction. The magnetic field of these objects is oriented along their major axis and they present polarized radiation. They are used as major merger tracers. The halos are cluster scale objects ($\sim 1\text{Mpc}$), at the center of the merging cluster, with a regular shape and without optical counterpart. They are not associated with galactic activities, they have low surface brightness and low polarization and they are associated with merger clusters. Mini-halos have a size comparable to the cooling radius of clusters ($\sim 100\text{-}500\text{ kpc}$), with low surface brightness, low polarization and no optical counterpart. However, they are not 'small' halos because they are not associated with merger events, but they are observed in cool-core clusters, or relaxed objects. They are probably the result of AGN feedback because the central BCG is always observed in their center;

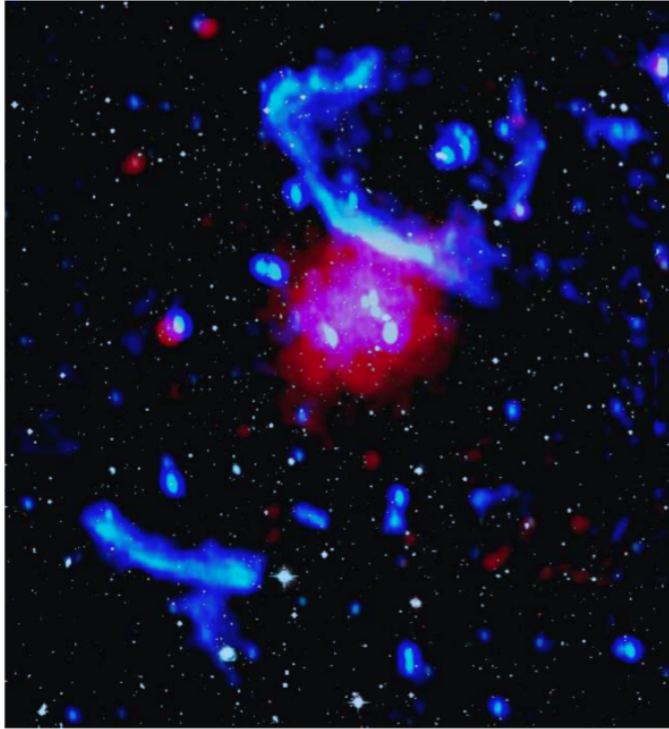


Figure 1.1: X-ray emission in red (XMM-Newton), radio emission at 323 MHz in blue (low resolution, beam FWHM $\sim 22'' \times 18''$) by [Bonafede et al. \(2014\)](#)

- **SZ effect:** this effect was proposed by [Sunyaev & Zeldovich \(1970\)](#). The thermal-SZ effect is caused by the inverse-Compton scattering between the thermal free electrons of the Intra Galactic Medium (IGM) ($10^5\text{-}10^8\text{K}$) and Cosmic Microwave Background (CMB) photons ($\sim\text{K}$). Photons gain energy

causing a distortion of the of Black Body (BB) spectrum of the CMB. The following picture shows how the spectrum is modified by the thermal SZ effect.

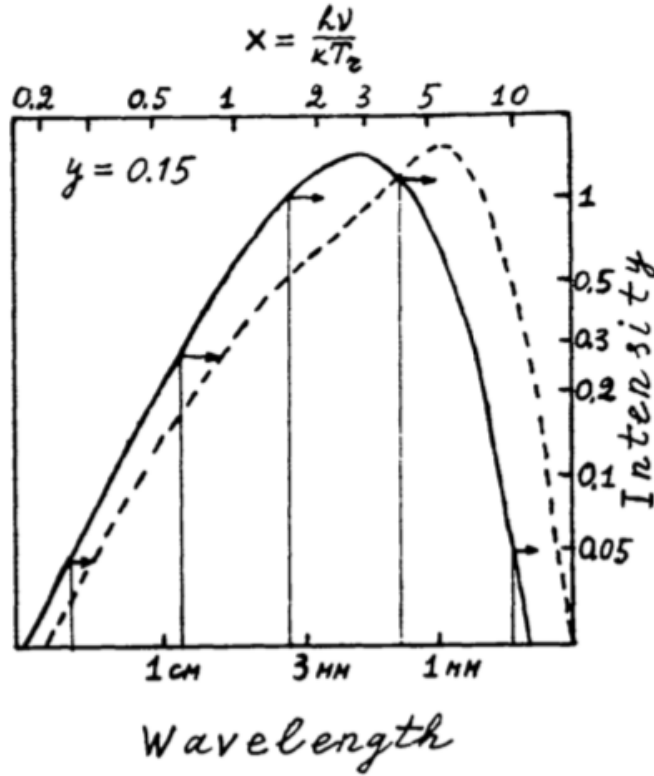


Figure 1.2: Original figure by [Sunyaev & Zeldovich \(1980\)](#). In solid line is shown the original CMB spectrum, while in dashed line is shown the spectrum after a multiple Compton scattering (i.e. the thermal SZ effect)

For a given direction in the sky, the distortion of the BB spectrum can be calculated as a function of the observational frequency and of the thermodynamical conditions of the gas along the line-of-sight. This effect is fully described by the dimension-less Compton y -parameter, which is defined as:

$$y \equiv \frac{k_b \sigma_t}{m_e c^2} \int n_e T_e dl$$

where the 'e' subscript we indicate electron quantities, k_b is the Boltzmann constant, σ_t is the Thomson cross section and c is the light speed. In order to use the SZ effect, we define two quantities derived from the parameter y which make the observations independent of distance. These quantities are:

$$Y \equiv \int_{\Omega} y d\Omega$$

$$\Upsilon \equiv d_A^2 Y$$

With these definitions we passed from y which is a superficial brilliance, to Y (Integrated y -parameter) which is defined as a flow and we have arrived at Υ (Intrinsic y -parameter) which is a luminosity. In this way a distance independent measurement can be obtained. The SZ effect is used to study high- z clusters, as it is independent of redshift, determine cluster mass and baryon content, and the outskirts regions of clusters can also be studied. In recent years, the Planck Satellite provided fundamental insight on the cosmological and physical properties of galaxy clusters, observed via the SZ effect (e.g. [Planck Collaboration et al., 2011, 2013](#))

1.3 ICM: Intra Cluster Medium

The Intra Cluster Medium (ICM) is plasma that permeates galaxy clusters. This plasma is heated to temperatures from 10^6 to 10^8 K and it is detectable through X-ray observations. It radiates energy through bremsstrahlung, a process that is proportional of temperature.

In order to study the physics of this plasma is useful to introduce the basis of our treatment: the Virial theorem, the self-similar scaling relation, the hydrostatic equilibrium.

1.3.1 Virial Theorem

In classical mechanics, the virial theorem binds the temporal mean of the kinetic energy and the potential energy of a stable system of N particles confined in a limited region of space. This can be applied to the study of galaxy clusters. The first formulation of this theorem is attributed to [Clausius \(1870\)](#).

To prove this theorem we start from the case of single particle of mass m , that is identified by position vector \vec{r} and subject to conservative force \vec{F} . We indicate with T its kinetic energy, we define A as follows and we calculate its temporal derivative:

$$\begin{aligned} A &= m \vec{v} \cdot \vec{r} \\ \frac{dA}{dt} &= m \frac{d\vec{v}}{dt} \cdot \vec{r} + m \vec{v} \cdot \frac{d\vec{r}}{dt} = \\ &= m \vec{a} \cdot \vec{r} + m v^2 = \\ &= \vec{F} \cdot \vec{r} + 2T \end{aligned} \tag{1.1}$$

F is a conservative force, $\vec{v} \cdot \vec{r}$, A , T and v^2 are limited. The temporal mean of $\frac{dA}{dt}$ tends to zero because:

$$\begin{aligned}
\left\langle \frac{dA}{dt} \right\rangle &= \lim_{\tau \rightarrow \infty} \frac{1}{\tau} \int_0^\tau \frac{dA}{dt} dt = \\
&= \lim_{\tau \rightarrow \infty} \frac{1}{\tau} \int_{A(0)}^{A(\tau)} dA = \\
&= \lim_{\tau \rightarrow \infty} \frac{A(\tau) - A(0)}{\tau} = 0
\end{aligned}$$

From the result just found and obtaining the time average of the equation 1.1 we found a relation between $\langle T \rangle$ and $\langle \vec{F} \cdot \vec{r} \rangle$:

$$\langle T \rangle = -\frac{1}{2} \langle \vec{F} \cdot \vec{r} \rangle$$

The amount that equals $\langle T \rangle$ is called virial of the particle.

In the case that F is a central conservative force, we can write the previous equation of function of T and the potential $U(r)$:

$$\begin{aligned}
\vec{F} &= -\hat{r} \frac{dU}{dr} \\
\langle T \rangle &= \frac{1}{2} \left\langle r \frac{dU}{dr} \right\rangle
\end{aligned}$$

If U is Coulomb attractive potential we obtain:

$$\langle T \rangle = -\frac{1}{2} \langle U(r) \rangle \quad (1.2)$$

1.2 relates the temporal mean of kinetic energy and the temporal mean of potential energy of the particle.

We now investigate the case of multiple particles. We define m_i and r_i as the mass and position of the i -th particle, the force must be divided in internal force $\vec{F}_{i,j}$ (where j identifies a particle different from i) and external force \vec{F}_i^{ext} . Similar to the case of a single particle, by introducing the summation on all the particles that form the system, we obtain a form for $\langle T \rangle$:

$$\langle T \rangle = -\frac{1}{2} \left\langle \sum_i \vec{F}_i^{\text{ext}} \cdot \vec{r}_i + \sum_{i < j} \vec{F}_{i,j} \cdot \vec{r}_{i,j} \right\rangle$$

We now define the average work of internal and external force and we get the final definition of $\langle T \rangle$:

$$\begin{aligned}\langle L^{\text{ext}} \rangle &= \left\langle \sum_i \vec{F}_i^{\text{ext}} \cdot \vec{r}_i \right\rangle \\ \langle L^{\text{int}} \rangle &= \left\langle \sum_{i < j} \vec{F}_{i,j} \cdot \vec{r}_{i,j} \right\rangle \\ \langle T \rangle &= -\frac{\langle L^{\text{ext}} \rangle + \langle L^{\text{int}} \rangle}{2}\end{aligned}$$

Gas subject to a field of central external forces, such as the ICM case confined by the cluster's gravitational potential, the contribution of internal forces is null and the formula above:

$$\langle T \rangle = -\frac{1}{2} \langle U \rangle \quad (1.3)$$

where now T is the total kinetic energy of the system and U is the total potential energy described by the summation $\sum_i U(r_i)$. In the following, we will see how this model can be extended to the case of "microscopic" kinetic energy (i.e. gas temperature) in the case of a collisional gaseous atmosphere.

1.3.2 Self-similar scaling relations

For the presentation of the scale laws and their function in relation to our work, we referred to the review [Gitti et al. \(2012\)](#) and the references therein.

Considering the formation of cosmological structures as a process originated from scale-free density and the thermodynamical properties of the ICM determined by gravity alone, as presented in the work by [Kaiser \(1986\)](#). Under these assumptions, galaxy clusters of different masses may be considered as a scaled version of each other.

This last statement is based on the fact that considering the proportionality between the total density ρ and the average density of the universe to given redshift, defining the parameter of overdensity Δ and the average density $\rho_{c,z}$ as:

$$\rho_{c,z} = \frac{3H_z^2}{8\pi G} \quad (1.4)$$

$$\Delta = \frac{\rho}{\rho_{c,z}} \quad (1.5)$$

Where H_z^2 is the definition of Hubble constant for a Universe Λ CDM:

$$H_z^2 = H_0 \sqrt{\Omega_m(1+z)^3 + \Omega_\Lambda} = H_0 E(z) \quad (1.6)$$

We obtain that all the clusters have the same properties if rescaled for Δ , factor of overdensity.

M_Δ and R_Δ as the mass and the radius at the critical density Δ , we obtain the first relation, which relates precisely mass and radius:

$$\begin{aligned} M_\Delta &\propto \rho_{c,z} \cdot \Delta \cdot R_\Delta^3 \\ M_\Delta &\propto \rho_{c,0} \cdot E(z)^2 \cdot \Delta \cdot R_\Delta^3 \\ R &\propto M^{\frac{1}{3}} \cdot E(z)^{-\frac{2}{3}} \end{aligned} \quad (1.7)$$

where the relation 1.7 is the so-called 'M-R relation'.

If we assume that the collapse of the gas inside the potential well is slow, it is regulated by the Virial equilibrium. We can relate the infall velocity and the temperature of the gas, applying the relations obtain by the Virial theorem (1.8) and by the kinetic theory of the gas (1.9):

$$\begin{aligned} m v^2 &= \frac{G M m}{r_{\text{vir}}} \\ v^2 &= \frac{G M}{r_{\text{vir}}} \end{aligned} \quad (1.8)$$

$$\begin{aligned} \rho v^2 &\propto \frac{\rho}{m_p \mu} k T \\ v^2 &\propto \frac{k T}{m_p \mu} \end{aligned} \quad (1.9)$$

Combing the previous relations, we obtain the following equation that which allows us to calculate the virial temperature of the cluster:

$$T_{\text{vir}} = \frac{G M \mu m_p}{k r_{\text{vir}}} \sim 10^8 [\text{K}] \quad (1.10)$$

where M is the total mass and r_{vir} is the virial radius.

The temperatures that are reached are so high that the gas emits in the X band. Recalling that that the brightness in this band is directly proportional to the square of the density, we obtain a sphere at hydrostatic equilibrium, for which we obtain the relationship between virial temperature and mass:

$$\begin{aligned} kT &\propto \frac{M}{R} \propto M^{\frac{2}{3}} \cdot E(z)^{\frac{2}{3}} \\ M &\propto T^{\frac{3}{2}} \cdot E(z)^{-1} \end{aligned} \quad (1.11)$$

where the relation 1.11 is the so-called 'M-T relation'. However, it is more useful to relate mass and temperatures with observable quantities. It is possible to relate brightness to the density of the gas:

$$L_x \propto \rho^2 \cdot \Lambda \cdot V$$

ρ is the average density of the gas and it is possible to consider it as a tracer for the dark matter density:

$$\rho \propto \rho_{DM} \propto \rho_{c,z}$$

Λ is the cooling function that for the temperatures we are considering it is dominated by the bremsstrahlung and it is proportional to square root of temperature. Under these assumptions:

$$L_x \propto \rho \cdot T^2 \cdot M$$

$$L_x \propto \rho_0 \cdot E(z)^2 \cdot T^{\frac{1}{2}} \cdot M$$

$$L_x \propto E(z)^2 \cdot T^{\frac{1}{2}} T^{\frac{3}{2}} \cdot E(z)^{-1}$$

$$L_x \propto T^2 \cdot E(z) \tag{1.12}$$

where the relation 1.12 is the so-called 'L-T relation'. By combining the 1.11 and 1.12 we obtain:

$$L_x \propto (M^{\frac{2}{3}} \cdot E(z)^{\frac{2}{3}})^2 \cdot E(z)$$

$$M \propto L_x^{\frac{3}{4}} E(z)^{-\frac{7}{4}} \tag{1.13}$$

where the relation 1.13 is the so-called 'M-L relation'. This relation suggests that the assumption of collapse guided by gravity alone is not entirely correct and the model must be modified to consider phenomena that alter the formation of the structure (e.g. residual gas motions, feedback from galaxies, etc.).

In particular works like Etori et al. (2004) suggest that the 'L-T relation' is much steeper than the self-similar predictions, changing the index of T from 2 to 2.5-3. This behavior requires a modeling that considers non-gravitational phenomena.

1.3.3 Hydrostatic model

The sound speed is:

$$c_s^2 = \frac{\gamma k T}{\mu m_p}$$

where $\gamma = \frac{5}{3}$ for a monatomic gas, hence we define the sound crossing time t_s as:

$$t_s = 6.6 \cdot 10^8 \left(\frac{T}{10^8 \text{ K}} \right)^{-\frac{1}{2}} \left(\frac{D}{1 \text{ Mpc}} \right) [yr]$$

where D is the cluster's diameter.

First approximation we can consider the cluster age of the order of 10^{10} year and we note that the t_s is shorter than cluster age. We can therefore apply the hydrostatic equilibrium to model the ICM profile.

This model assumes that the gas is in hydrostatic equilibrium in the gravitational potential of the cluster and the pressure gradient is determined by:

$$\nabla p = -\rho \nabla \phi \quad (1.14)$$

where ϕ is the gravitational potential of the cluster and p is the gas pressure and it is defined as:

$$p = \frac{\rho k T}{\mu m_p}$$

If we assume that the gas is homogeneous and the cluster is spherically symmetric, the equation 1.14 reduces to:

$$\frac{1}{\rho} \frac{dp}{dr} = -\frac{d\phi}{dr} = -\frac{G M(r)}{r^2} \quad (1.15)$$

where r is the radius from the cluster center and $M(r)$ is the mass within r .

From the equation 1.15 and assuming $T=T(r)$ and $\phi=\phi(r)$, we can estimate the total mass of the cluster within r from the following equation:

$$M_{\text{tot}}(< r) = -\frac{k T r}{G \mu m_p} \left[\frac{d \ln \rho}{d \ln r} + \frac{d \ln T}{d \ln r} \right] \quad (1.16)$$

The equation 1.16 is used to estimate the cluster total mass from X observation, from which is possible to obtain density and temperature radial profiles.

Both results obtained with simulations (Rasia et al., 2006; Piffaretti & Valdarnini, 2008) and observational tests (Voigt & Fabian, 2006; Ghirardini et al., 2017) show how the hydrostatic model underestimates the cluster total mass. This suggests the

need to introduce non-thermal pressure terms and to consider the ICM as a non-equilibrium gas.

An application of hydrostatic model was proposed in [Cavaliere & Fusco-Femiano \(1976\)](#). In this work the authors hypothesize that gas and galaxies are in equilibrium in the same gravitational potential and using the King's approximation for the galaxies distribution ([King, 1962](#)), they obtain the so-called ' β model'. In this model the density profile is written as:

$$\rho(r) = \rho_0 \left[1 + \left(\frac{r}{r_{\text{core}}} \right)^2 \right]^{-\frac{3}{2}\beta}$$

where the parameter β is defined as:

$$\beta = \sigma_r^2 \cdot \frac{\mu m_p}{k T} \quad (1.17)$$

where σ_r is the line-of-sight velocity dispersion and represents the ratio of specific kinetic energies of galaxies and gas. Using the equation 1.17 is possible to obtain the following analytic form to calculate the cluster total mass:

$$M_{\text{tot}}(< r) = \frac{k r^2}{G \mu m_p} \left[\frac{3 \beta r T}{r^2 + r_{\text{core}}^2} - \frac{dT}{dr} \right] \quad (1.18)$$

This model still presents issue, particularly in the description of the cool-core cluster, clusters that exhibit peculiar behaviors in the innermost region of their volume.

Because of the importance of mass estimation for cosmology, it is necessary for the models to be able to give the most accurate predictions. It is therefore necessary to understand non-gravitational terms, such as AGN contributions or turbulent motions, which will be in the next chapter.

Chapter 2

Turbulence

In the previous chapter we have shown that simplistic models based on the hydrostatic equilibrium of the ICM are not good enough to explain the variety of dynamical processes observed in X-ray and radio waves. Therefore, it is useful also to include a description of what residual gas motions (naturally produced by a number of mechanisms present in galaxy clusters) can do in the intracluster medium. The most successful (and simplistic) model of turbulence is the "Kolmogorov model", that it is an important mathematical simplification and, under a few limiting physical assumptions on the behavior of the gas, it can also give reasonable expectations about the evolution of turbulent gas motions in the plasma of galaxy clusters.

The intents of this chapter are the introduction of turbulence and the presentation of modern results of simulations and observations of turbulent motions in ICM.

2.1 Theoretical bases

Describing in a complete and exhaustive way the ICM implies the study of the turbulent motions that are generated in the continuous gravitational interactions in the whole evolutionary history of the clusters. The models presented below are the Kolmogorov theory and Ram Pressure Stripping.

The first can be applied to most type of gas dynamics study and it is particularly useful because under a few but fundamental assumptions it can describe analytically the behavior of the gas.

Baseline Kolmogorov theory for turbulence

The first formulation of this theory is by [Kolmogorov \(1941\)](#) but in this work we used the formalism presented in the book 'Astrophysical Hydrodynamics: An Introduction' written by [Shore \(2007\)](#).

The assumptions that underlie Kolmogorov's theory are:

- fluid is solenoidal: $\vec{\nabla} \cdot \vec{v} = 0$ (i.e. the fluid is incompressible)
- steady state
- fully developed turbulence
- the fluid is homogeneous and isotropic

Under these assumptions turbulence is described by "eddies". The role of the latter is fundamental because it is through them that the energy fed into the system on large-scale eddies is dissipated, through a cascade, to smaller and smaller eddies, until the energy is dissipated into heat.

We identify with ϵ the rate of energy dissipation and with ν the coefficient of molecular viscosity. The Reynolds number of the medium is:

$$\text{Re} = \frac{U L}{\nu}$$

where U is the typical velocity of the fluid at the typical scale L . What follows from these assumptions is a velocity structure that will be independent of the length scale and we can use dimensional analysis to obtain its form.

Dimensionally ϵ is $L^2 T^{-3} = U^3 L^{-1}$ and it is constant for:

$$u_l = \epsilon^{\frac{1}{3}} l^{\frac{1}{3}}$$

In turbulence regime the viscosity is given by:

$$\nu = u_l l = \epsilon^{\frac{1}{3}} l^{\frac{4}{3}}$$

The upper length scale is determined by the size of the energy source. On the other hand the minor length is the scale where the viscous time scale becomes equal to the eddy turn-over time:

$$l_K = \left(\frac{\nu^3}{\epsilon} \right)^{\frac{1}{4}}$$

where we use the subscript 'K' to indicate the Kolmogorov (or dissipation) length for which the characteristic velocity is:

$$v_K = (\nu \epsilon)^{\frac{1}{4}}$$

At the Kolmogorov length the energy transfer becomes irreversible. We can also define a time scale related to the Kolmogorov length:

$$t_K = \left(\frac{\nu}{\epsilon}\right)^{\frac{1}{2}}$$

Having defined these fundamental quantities, we can now state the main application of Kolmogorov theory. There is a range of length over which turbulence spectra appear to be “universal”, they do not depend on the properties of the medium with which one is dealing. However, the energy spectrum is still linked to the viscosity of the medium:

$$E(k, t) = \nu_K^2 E_*(l_K k)$$

where E_* is a universal dimensionless function of the wave number and k is the wave number related with eddies length ($k = \frac{2\pi}{l}$). The form of the spectrum is given by:

$$\epsilon = -\frac{3}{2} \frac{du^2}{dt} = 2\nu \int_0^\infty E(k, t) k^2 dk$$

Substituting our dimensional analysis:

$$E(k, t) \sim \epsilon^{\frac{2}{3}} k^{-\frac{5}{3}} \quad (2.1)$$

The relation 2.1 is the Kolmogorov Power Spectrum. Therefore, in a wide range of scales between the injection and the dissipation of turbulent eddies (called the "inertial range", see figure 2.1), the spectrum can be considered universal, and it is independent of the mechanism responsible for its ultimate dissipation into heat. The population of eddies of a given region of the spectrum remains constant over time because the larger eddies are separated in smaller eddies and this considering also the cascade effect, keeps constant the number of eddies of fixed size. The following plot shows the energy spectrum as a function of the wave number and it shows that at a smaller size of the Kolmogorov scale (major k) the energy is entirely damped by the dissipation effect.

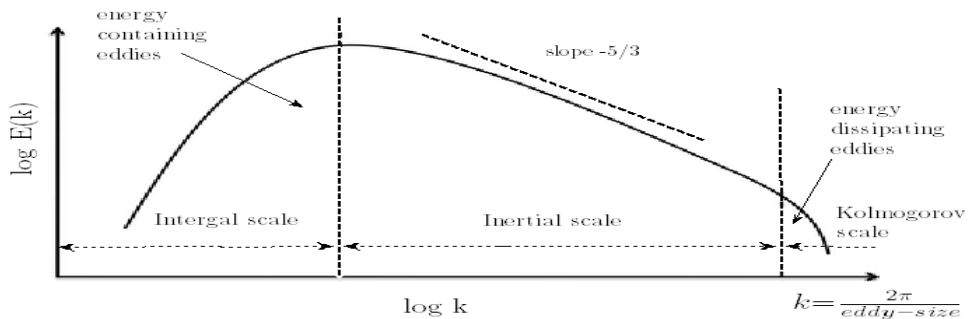


Figure 2.1: Energy spectrum as a function of the size of the eddies (Sinha, 2013)

Beyond the Kolmogorov model

In order to study real, low-density and possibly magnetised gas the assumptions which are at the base of Kolmogorov model can not be used and it is necessary to generalize the model, having to deal with the turbulence in a qualitative way, as it is not possible to give an analytical description. In this section we discuss the cases of supersonic, magneto hydrodynamic, self gravitating and no steady-state turbulence.

The case of non stationary turbulence was studied by [Kolmogorov \(1962\)](#). In this paper the author expanded his model including the evolution of the power spectrum with time. The assumption of steady-state is verified when the source of turbulence is continued, but if its effect break down, the power spectrum evolves as:

$$\int E(k, t) k^2 dk \sim t^{-\frac{5}{2}} \quad (2.2)$$

This relation became from the analysis of the moment of the turbulent velocity in Fourier space and the introduction of the two-point correlation function in the following form:

$$R_{i,j}(r) = \frac{(2\pi^3)^{\frac{1}{2}}}{16[\nu(t-t_0)]^{\frac{5}{2}}} \left[C_{ijll} - C_{ijlm} \frac{r_l r_m}{4\nu(t-t_0)} \right] \exp\left(-\frac{r^2}{8\nu(t-t_0)}\right) \quad (2.3)$$

where C_{ijll} and C_{ijlm} are constants. The turbulence correlation function, and as a result the energy, therefore decays according to:

$$R_{i,j}(r) \sim [\nu(t-t_0)]^{-\frac{5}{2}} \exp\left(-\frac{r^2}{8\nu(t-t_0)}\right) \quad (2.4)$$

and so we obtain the integral relation in the equation [2.2](#).

Kolmogorov thus described the power spectrum in case of unsteady state as:

$$E(k) = E_0 k^{-\frac{5}{3}} \exp\left(-\frac{3}{2} \alpha k^{\frac{4}{3}} \nu \epsilon^{-\frac{1}{3}}\right) \quad (2.5)$$

where α is a universal constant and E_0 is the normalization of the spectrum. In this form the spectrum is essentially the same of the state-steady case, but there is a characteristic wave number which is the point where the assumption of Kolmogorov theory breaks down and it also represents the critical scale for the generation of cascades. This characteristic wave number k_* is:

$$k_* = \left(\frac{2}{3\alpha}\right)^{\frac{3}{4}} \left(\frac{\epsilon}{\nu^3}\right)^{\frac{1}{4}} \quad (2.6)$$

We write the equation for the spectral evolution of the turbulence as

$$\frac{\partial E(\mathbf{k}, t)}{\partial t} = T(\mathbf{k}, t) - 2\nu k^2 E(\mathbf{k}, t) \quad (2.7)$$

where T is defined as

$$T(\mathbf{k}, t) = 4\pi k^2 \int \mathcal{Q}(\vec{\mathbf{k}}, \vec{\mathbf{k}}', t) d\vec{\mathbf{k}}' \quad (2.8)$$

and \mathcal{Q} is the dissipation rate. The steady-state turbulence gives $T=2\nu k^2 E$. We introduce now the magneto hydrodynamic turbulence. Magnetic fields on the large scale can couple distant parts of the fluid, thus violating the simple locality assumption which we used for the Kolmogorov theory. Alfvén waves can transfer energy away from an eddy faster than it can be otherwise dissipated by viscosity and, therefore, the energy dissipation rate gets faster than in the simpler Kolmogorov's model. In order to find the power spectrum in presence of magnetic field we analyze the typical velocities which characterize the phenomena, Alfvén speed v_a and the velocity associated at wave number v_k . In particular we compare the characteristic time scale of coupling, which is defined as L/v_a and which describes the typical time in which a Alfvén wave connects two gas zones located at distance L (i.e. the magnetic crossing time), and the hydrodynamic time scale, which describes the eddy turnover time and which is defined as $1/(k v_k)$. When these times are comparable, we can describe the power spectrum as:

$$E(\mathbf{k}) \sim \frac{v_a}{l_0} k^{-\frac{3}{2}} \quad (2.9)$$

where l_0 is the length associated at the wave number which equals the times scale above defined. This spectrum is the Kraichnan spectrum which was described for the first time by [Kraichnan \(1965\)](#).

More recent studies also included, it was introduced the intrinsic anisotropy of the cascade. This is introduced by the assumption that the time scale for orthogonal scattering l_{\perp}/v_l is approximately the same as for parallel, l_{\parallel}/v_a , and since $\epsilon = v_a^3/L$. With these dependences, the eddies become more elongated with decreasing length, because $k_{\perp}/k_{\parallel} \sim (Lk_{\perp})^{\frac{1}{3}}$. Numerical simulations show that, on the smallest scales, the turbulence becomes extremely filamentary and intermittent. An other fundamental result is that for the perpendicular direction the power spectrum has the same slope of the spectrum presented by [Kolmogorov \(1941\)](#). In the parallel direction, however, the spectrum is steeper:

$$E(k_{\parallel}) \sim (\epsilon^3 v_a^{-5})^{\frac{1}{2}} k_{\parallel}^{-\frac{5}{2}} \quad (2.10)$$

If the turbulent region becomes supersonic, internal shocks become the primary mode for dissipation. From simulations and experiments it is found that strongly compressed regions develop, with high vorticity, at high-flow Mach numbers, and

the medium rapidly evolves into localized structures. Some of these regions move with bulk supersonic velocities, but as they collide and the overall temperature rises and thus the motions become progressively more subsonic. The contact surfaces are formed by the intersections of shocks. These will form on collision of the turbulent eddies and locally planar fronts within a supersonic medium. The results of these interactions is the injected vorticity which is, however, on a small scale. Unlike the Kolmogorov model, these do not necessarily proceed from the large-scale structures through a cascade to smaller scale. The inertial range does not exist in these conditions.

The most important difference between supersonic and subsonic turbulence is found in magneto-hydrodynamics (MHD) turbulence. In this case initially supersonic, but sub-Alfvénic, modes propagate nonlinearly and turn into internal shocks and the energy is rapidly dissipated. The main results are obtained from simulations, which reported that there are many relations between dynamical helicity and magnetic helicity. These relations indicate that the local vorticity (an indicator of turbulence) is influenced by the structure of the overall field.

From the study of Molecular Clouds emerges that their structure and internal velocities are supported by supersonic turbulence. Indeed, the observed velocity dispersions in molecular lines are often a few kilometers per second which are greater than the typical sound speed in molecular clouds. However, the motions are dissipative because the clouds can radiate their turbulent energy in the infrared and millimeter. The waves that are developed in the medium are turbulent and they develop a pressure term which is added to total pressure support. This type of support is called self-gravitating turbulence and its study is just beginning with the two- and three-dimensional modeling.

In summary, given the above variety of models for turbulence, we expect that turbulence in the intracluster medium can display a variety of interesting (and complex) features, which are not fully captured by a unique model. The intracluster medium is indeed internally stratified (we observe a density radial profile), shaken by non-stationary motions which can inject turbulence across different scales, alternatively in subsonic or transonic regime depending on its merger state, and also affected by magnetic fields, which can locally become dynamically dominant.

2.2 Turbulence in galaxy clusters

For a long time the modeling of the ICM has relied on the simplistic assumption that proton-proton collisions were the leading mechanism of energy exchange, thereby suggesting that the Coulomb mean free path sets lower limit for the size of hydrodynamical features in the ICM:

$$\lambda_p \approx \lambda_e = \frac{3^{\frac{3}{2}}(kT)^2}{8\sqrt{\pi}n_e e^4 \ln(\Lambda)} \simeq 23 \left(\frac{T}{10^8 [\text{K}]} \right)^2 \left(\frac{n}{10^{-3} [\text{cm}^{-3}]} \right)^{-1} [\text{kpc}] \quad (2.11)$$

where n is the number density of the gas.

Under this hypothesis, the ICM should be very viscous as its Reynolds number should be rather small (see [Roediger & Brüggen \(2008\)](#) and references therein):

$$\text{Re} = \frac{\text{UL}}{\nu} \sim \frac{v_{gas} \cdot \lambda}{\mu / \rho_{gas}} = \frac{[cm \ s^{-1}] \cdot [cm]}{[g \ cm^{-1} \ s^{-1}] / [g \ cm^{-3}]} \quad (2.12)$$

and if we consider the typical values for the ICM, we obtain:

$$\text{Re} = \frac{\text{UL}}{\nu} \sim \frac{v_{gas} \cdot \lambda}{\mu / \rho_{gas}} \sim \frac{10^8 \cdot 10^6 \cdot 3,08 \cdot 10^{18}}{10^3 / 10^{-27}} \sim 100 \quad (2.13)$$

where μ in equation 2.13 is the relevant coefficient of viscosity which is given by [Braginskii \(1958\)](#) and [Spitzer \(1962\)](#) and it is:

$$\mu \approx 6.0 \cdot 10^{-17} \cdot \left(\frac{\ln \Lambda}{37} \right) \cdot T^{\frac{5}{2}} \left[\frac{\text{g}}{\text{cm s}} \right] \quad (2.14)$$

Therefore, such a modest Reynolds number implies that in the ICM an instability hardly evolves in turbulence and the motions tend to remain laminar.

More recently, many authors have studied the role of magnetic field in proton-proton interactions and how the presence of magnetic fields varies the compute of viscosity. In particular in a recent paper by [Beresnyak & Miniati \(2016\)](#), it is discussed how the presence of amplified magnetic fields should reduce the effective mean free path of ICM protons from 20 kpc to \ll kpc, thus greatly reducing the effective viscosity of the ICM. The presence of small-scale velocity and magnetic fluctuations in the ICM is also indirectly supported by a number of high resolution X-ray (e.g. [Zhuravleva et al., 2014](#); [Hitomi Collaboration et al., 2016](#)) and radio observations (e.g. [Bonafede et al., 2010](#); [Rajpurohit et al., 2018](#)), suggesting the presence of ICM fluctuations at least down to \sim kpc scales. With typical value of gas velocity and cluster's dimension we can calculate the Reynold's number for ICM and we find value between 10^6 and 10^{29} . These values are orders of magnitude larger than 10^2 , the minimum value of Reynold's number that it is normally used to defined a turbulence medium.

Based on the above expectations, it is clear that ICM is a gas where a little instability can evolve to became a turbulence motion very easily, which motivates the idea that turbulence can indeed be an ubiquitous source of pressure support in galaxy clusters.

2.2.1 Ram Pressure Stripping

Minor and major mergers occur in clusters have a fundamental role of dynamical quantities. In the study of turbulence motions is important to characterize phenomena called Ram Pressure Stripping. For the treatment of this phenomenon we rely on the description given by [Cassano & Brunetti \(2005\)](#).

The typically velocity of the passage of the in-falling sub-halos through the main cluster during mergers induces large-scale bulk flows of the order $\sim 1000 \text{ km s}^{-1}$. The crossing of the sub-halos in the volume of primary cluster induces in ICM eddies by Kelvin-Helmoltzs instability. These eddies, in few Gyr, redistribute the energy of merger in cluster volume by injecting random and turbulent velocity fields. Depending on the initial conditions and on the mass ratio of the two sub-clusters, during the merging process the in-falling halos may be efficiently stripped due to the ram pressure. The sub-halo is stripped until the equipartition between static and ram pressure is established, which allows writing:

$$\bar{\rho}_{\text{max}} v_i^2 = \frac{\rho_{\text{min}}(r_s) k_b T_{\text{min}}}{\mu m_p}$$

where 'min' it refers to sub-halo quantities, while 'max' it refers to main cluster quantities. The velocity v_i is the relative impact velocity between cluster and sub-halo.

The injection rate per unit volume of turbulence is predicted to be:

$$\frac{E_t}{\tau_{\text{cross}} \times V_H} \simeq \frac{\bar{\rho}_{\text{max},s}}{R_{\text{max}}} v_i^3 \left(\frac{V_t}{V_H} \right) \quad (2.15)$$

where the main quantities in the equation 2.15 are the total energy E_t injected in turbulence during a merger event and the ratio between the volumes of the cluster and sub-halo. Indeed, the velocity of the impact is determined for the most part by the mass of the cluster and it is about the same for all the mergers, so the energy injected is determined by volume of the clump in in-fall.

Total energy injected in ICM by mergers is about 10-15 per cent of the thermal energy, that is obtained by 'M-T relation' (see the relation 1.11).

This result is also confirmed by simulations and observations, as we also analyze in this thesis in the next paragraphs. Exactly which fraction of this energy gets channeled into turbulent motions is more difficult to predict, and this motivates the role of numerical simulations in the detailed study of turbulence in the intracluster medium.

2.2.2 Injection of turbulence by shocks

Shocks can, both, inject or amplify vorticity in a fluid, and are therefore an important contributor to the overall evolution of turbulence in the ICM (e.g. [Porter et al., 2015](#)). In [Vazza et al. \(2017\)](#) and [Wittor et al. \(2017\)](#) the authors present results on the generation of solenoidal and compressive turbulence in the ICM. Their work focused in different type of filtering which can be used in study of turbulent velocity. They decomposed the velocity in two different contribution: solenoidal motions and compressive motions. The first ones are responsible for stretching and folding of the structure and they influence the evolution of magnetic field, while the second ones are responsible for the generation of weak shocks, which in turn generate solenoidal motions. In order to avoid spurious terms induced by shocks, the authors apply the same shock finder algorithm that we use in this work, which is presented in [3.2](#).

As shown in [Vazza et al. \(2017\)](#), the shocks affect both the solenoidal motions and the compressive ones. Weak merger shocks are often associated with true turbulent motions, while strong shocks and those whose extents exceed the cluster core scales do not generate turbulent motions.

It is, however, non trivial separate which shocks generate turbulence and which instead do not generate non-thermal pressure contributions. There are some algorithms able to identify the presence of shocks that generate turbulence and to mask them, such as the one presented in the section [3.2](#).

2.2.3 Injection by AGN

A further source of turbulence in the ICM is represented by the central Active Galactic Nuclei (AGN). This contribution is originated by the interaction between the feedback mechanisms of the central Black Hole (BH) and the gas which surrounds the core. As discussed by many authors, also using numerical simulations (e.g. [Brighenti & Mathews, 2002](#); [Brüggen, 2003](#); [Gaspari et al., 2011](#)) the injection of turbulence by AGN feedback is relevant for the evolution of different astronomical objects, from this source of turbulence can be studied in very different astronomical objects, from massive galaxies to galaxy clusters.

Recently, [Gaspari et al. \(2018\)](#) presented a model based on the top-down multi-phase condensation. In this model hot and warm phases coexist. The hot gas is contained in hot gaseous halos, while warm gas is organized in filaments which are composed by a combination of ionized and neutral medium. The hot halos are perturbed by subsonic turbulence, while the filaments are able to condense out of the turbulent eddies and increase very efficiently on the central BH. The authors show that this type of accretion, which is call Chaotic Cold Accretion (CCA), is about ~ 100 times more efficient than Bondi's accretion. This phenomenon is

self-regulated and causes alternating phases of efficient accretion with the related feedback mechanisms, for which the turbulence is sub-dominant, and phases for which the turbulent motions are instead to support the gas structure.

The multiphase nature of the gas is very important because it is difficult to study the hot phase for the low spatial resolution of the X-ray telescopes, while the warm phase is studied with IR or radio observation for which the spatial resolution allows to studied the internal kinematic of the gas. Probably the main result for the internal kinematic in hot gas was obtained by the observation of the Persus cluster by the Hitomi space telescope. In [Hitomi Collaboration et al. \(2016\)](#) (see also section 2.4 below) the authors presented the results obtained by studying the line-of-sight velocity dispersion in central region of Perseus and they found that this value is ~ 160 [km s⁻¹] on scales of a ~ 50 kpc, which is less than what is required to balance the gas cooling rate in this region solely by dissipating turbulent kinetic energy. This suggests that in the core of the cluster, the turbulence energy dissipation is not the primary heating of ICM and that only the study of multiphase gas can be explain the real nature of the ICM, especially in the central region of the clusters.

2.3 Simulated turbulence in the ICM

Below we discuss the results of the current numerical simulations about turbulence in ICM. As we explained in previous paragraphs, these simulations resolve the numerical equations and the results are the time dependent solutions of the behavior of the gas.

Probably the first work which studied the statistical properties of ICM was presented in [Norman & Bryan \(1999\)](#). In this paper the authors presented the results obtained from high resolution hydrodynamic simulations of the formation and evolution of X-ray clusters of galaxies. They used the accurate Piecewise Parabolic Method (PPM) on fixed and adaptive meshes which allow them to resolve the flow field in the intracluster gas. They found that the turbulence is strongest in the outskirts of the cluster and weaker in the core, with values which are about $\sim 25\%$ of σ_{vir} (where σ_{vir} is the value of velocity dispersion at virial radius) in the core and about $\sim 60\%$ in the outskirts. They argued that the major mergers are more infrequent and so they can not sustain the observed level of turbulence in the core. They discussed two possible ways which can explain the value of turbulence in the core. The first is associated to the energy which is dissipated in ICM by the shocks, but the authors showed that this possibility generates a turbulent velocity which is less than the value which they observed. The second way, which they consider more likely, is that the turbulence is driven by the more frequent minor mergers.

[Dolag et al. \(2005\)](#) developed a new way to study the numerical viscosity in smoothed particle hydrodynamics (SPH) simulations. In a set of nine high-resolution simulations of cosmological galaxy cluster formation, they found that low-viscosity formulation of SPH produces higher levels of turbulent gas motions in the ICM. The kinetic energy content in random gas motions was up to 5–30 per cent of the thermal energy content, depending on cluster mass. This also has significant effects on radial gas profiles and bulk cluster properties. They shown that this type of viscosity can be used to study in more efficient way the shocks and the turbulent energy content. They found a turbulent energy content up to 30 percent (about 50 percent in the inner part of the massive clusters) and they shown that this content influenced many physical quantities as density, X-ray luminosity and the shape of metal lines observable with high-resolution X-ray spectrographs. The main result of this paper is the first power spectrum of the turbulence which shown how the turbulent content in simulated ICM change with the scale.

[Ryu et al. \(2008\)](#) studied the relation between turbulence and vorticity. They studied three-dimensional power spectra found in the simulation. They decomposed the velocity in three components and they focused their study in the vorticity component. They found a clear trend for the vorticity when they compared vorticity and the local eddy turnover time. In particular they found that the vorticity is larger at higher gas density and temperature. They also noted that after a few turnover time, vorticity decays and develops into turbulence. Finally, they suggested that the turbulence in clusters that was induced by the cascade of vorticity can amplify magnetic fields from seeds of any possible origin through stretching, twisting, and folding, the process known as turbulence dynamo.

[Lau et al. \(2009\)](#) studied the hydrostatic mass bias in a sample of 16 simulated galaxy clusters. They focused on the effects of residual gas motions on the estimates of the total mass of clusters. They analyzed systems that appear morphologically relaxed and perturbed in mock Chandra X-ray images separately to study the effects of dynamical state of clusters on the resulting mass. They found that gas motions contribute up to 5%–15% of the pressure support in relaxed clusters, which leads to the underestimate of the total virial mass in the hydrostatic analysis accounting only for the thermal pressure. On average they found that for relaxed systems the mass is underestimated by 6%-8% while at the same radii, for perturbed systems the mass is underestimated by 9%-11%. The authors suggested that this bias can be explain with turbulent motions of ICM, but it is also necessary take in account the role of cosmic rays and magnetic field as terms of non thermal pressure.

[Vazza et al. \(2011\)](#) studied the profiles and the power spectrum of turbulent motions as a function of dynamical state of the clusters. They used a sample of 20 simulated galaxy clusters, using the adaptive mesh refinement code *ENZO*. They developed

two methods to detect turbulent motions in the ICM. One is based on a filtering in the Fourier space of the component of velocities associated with wave numbers larger than the wavenumber of the maximum spectral energy, and the other is based on the filtering in the real space of the velocity component with coherence scales smaller than the fixed length of l_{\max} . They showed that the results are independent of the particular method adopted. They also found that post-merger and merging clusters have large values of turbulent energy compared to the thermal energy of the ICM, with a ratio $E_{\text{turb}}/E_{\text{therm}} \sim 0.2-0.3$ in the innermost cluster regions. On the other hand, relaxed clusters show much lower values of the turbulent ratio, $E_{\text{turb}}/E_{\text{therm}} \sim 0.05$ within the same radius. Thanks to the very high dynamical range, the authors also studied the power spectra of the 3D velocity fields extend across nearly two orders of magnitude. They shown that the energy $E(k)$ is proportional to $k^{-\frac{5}{3}-2}$, and the typical scale for the peak of the energy spectrum at the scales of $1-2 R_{\text{vir}}$, with the tendency of merging clusters to extend across the largest outer correlation scales.

This thesis extend some of the methodologies developed in this paper to a more recent and resolved set of simulations, and also introduces more sophisticated analysis techniques to identify turbulence in such simulations.

2.4 Observational indications of turbulence in the ICM

After the discussion of theoretical results, it is useful to present the observational evidences of turbulence in real galaxy clusters. The observations that are used in this studies are mainly carried out in the X-band and they present considerable difficulties due to the low resolution of the space telescopes.

Probably the first observational work constraining turbulence in ICM was [Schuecker et al. \(2004\)](#). In this paper the authors studied spatially-resolved gas pseudo-pressure maps of the Coma galaxy cluster, which are obtained from a mosaic of XMM-Newton observations in the scale range between a resolution of 20 kpc up to 2.8 Mpc. Using the Fourier analysis they found that for scales from 40 to 90 kpc the power spectrum of the pressure was well described the Kolmogorov power spectrum. This suggests that the pressure in this scale range is supported by turbulent pressure and they give a lower limit to this support, of about ~ 10 percent. They also computed the value of kinematic viscosity and they give a reliable upper limit of $\nu < 3 \cdot 10^{29} \text{ [cm}^2 \text{ s}^{-1}\text{]}$, for turbulent velocity of $250 \text{ [km s}^{-1}\text{]}$ at scale of $\lambda=100 \text{ kpc}$ and Reynolds number of 20. This suggests that in ICM a instability can easily develop turbulence. This work suggests that the turbulence in ICM can explain some observational bias and in the following years many other groups have improved observational techniques to further investigated these issues.

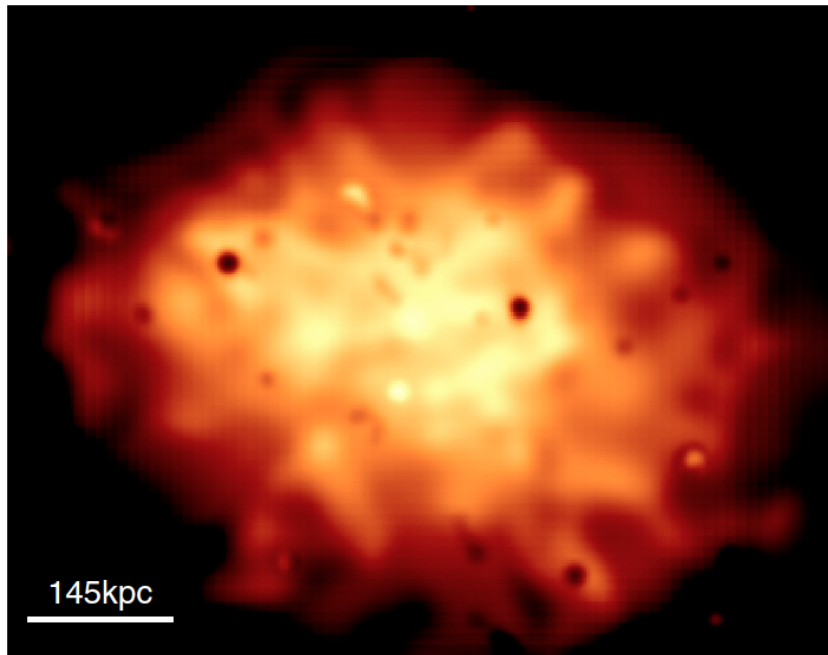


Figure 2.2: Detailed view of the projected pressure distribution of the central region of the Coma cluster, presented by [Schuecker et al. \(2004\)](#) and observed with XMM-Newton. The 145 kpc scale corresponds to the largest size of the turbulent eddies indicated by the pressure spectrum. The smallest turbulent eddies have scales of around 20 kpc.

[Sanders et al. \(2011\)](#) used the width of emission lines in XMM-Newton Reflection Grating Spectrometer (RGS) spectra, and they constrained the turbulent velocities of the X-ray emitting medium in the cores of 62 objects, including also galaxy clusters. For objects which have significant turbulent broadening they used also Chandra spectral maps. The main result of this work is that there is a little evidence for an extra broadening in the emission lines due to turbulence. Only for 15 sources they could limit the contribution of turbulent energy below 20 per cent of the thermal energy.

The main contribute at the study of turbulence in galaxy clusters was given by the space mission JAXA Hitomi X-ray Observatory, launched in February 2016. Hitomi worked over an energy range of 0.3-12 keV with X-rays focused by a mirror with angular resolution of 1.2 arcmin (HPD). The main characteristic of the space telescope Hitomi was its calorimeter which was cooled to 0.05K and this cooling allowed the detection of a Full Width Half Maximum (FWHM) of emission lines of 4.9 eV. This allowed to separate the contributions at gas velocity in thermal support, Doppler effect and many other terms, among which turbulent support.

In [Hitomi Collaboration et al. \(2016\)](#) the results of the study of gas dynamic in Persus cluster were discussed. In particular they found that the contribution at gas velocity from the turbulent motions is about ~ 160 [km s $^{-1}$] on scales of ~ 50 kpc. This suggests that in the central region of the cluster, the turbulent motions give a small contribution at the total pressure and that the turbulent pressure is given by the central AGN. Unfortunately, the space mission was supposed to perform several observations on the gas dynamics in the clusters, but ended earlier than expected.

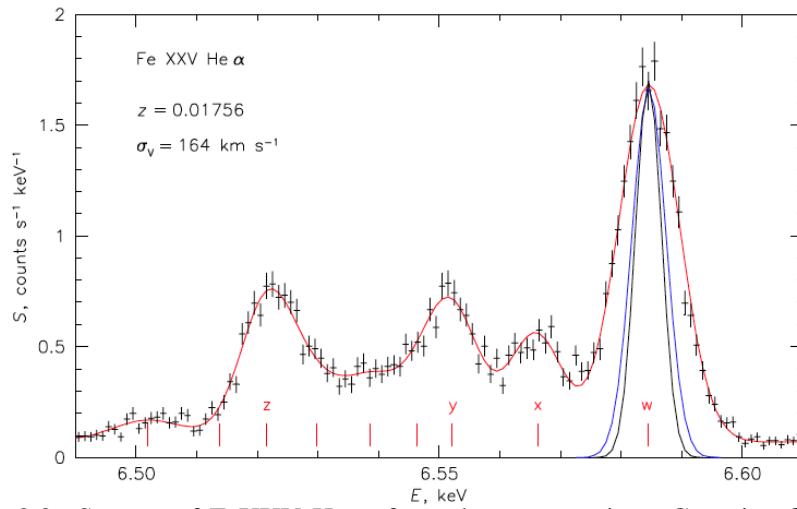


Figure 2.3: Spectra of FeXXV He- α from the outer region. Gaussian fits have been made to lines with energies (marked in red) from laboratory measurements in the case of He-like FeXXV, Instrumental broadening with (blue line) and without (black line) thermal broadening are indicated. The redshift is the cluster value to which the data were self-calibrated using the He- α lines. The strongest resonance (w), intercombination (x,y) and forbidden (z) lines are indicated. Spectra from paper [Hitomi Collaboration et al. \(2016\)](#)

Chapter 3

Numerical Analysis

In this chapter we will present main part of the code that we created for our analysis. We focus on the parts of the code which mostly influences scientific understanding of the results we will achieve. In appendix [A](#) we explain the whole workflow of our code which explains the whole analysis and its characteristic.

3.1 Effects of the filtering scale on turbulence

In this Section we test our filtering techniques for turbulence using a typical simulated galaxy cluster (with a mass of $7.12 \cdot 10^{13} M_{\odot}$ at $z=0$), taken from the cluster sample described in section [4.1](#). The output is made of 320^3 cells, with a fixed resolution of 20 kpc, centered on the cluster center of mass.

To disentangle turbulent motions from bulk motions, it is useful to use define a small-scale filtering approach. In this approach the turbulence velocity is approximated as the part of the 3D gas velocity that fluctuates on the smallest scales. This makes sense because turbulence motions interest small regions of the cluster and if we will find motions on large scale, it is possible to evaluate this like bulk motion of the gas. Most of the turbulence we expect to detect in the internal region of galaxy clusters should follow from the mixing of ram-pressure stripped gas, as we already presented in the paragraph [2.2.1](#).

With the use of a small-scale filter, it is possible to define the velocity of the bulk motions and to calculate the velocity of the turbulence motions like the difference between total velocity and bulk ones.

In particular we used scales of 60, 100, 200, 400 e 600 kpc and the GDL's procedure SMOOTH.PRO. The drawback of this procedure is that the velocity fluctuation cannot be defined for cells at a distance $\leq \Delta$ from the edge of the computing volume, where Δ is the assumed filtering scale.

The study of different scales allowed us to identify the best scale that enables the

identification of turbulence motions. In the following plots, the profiles of the thermal energy and kinetic energies associated at two different velocity fields are reported with name 'Turbulence', energy calculate with smoothed velocity, and with 'Kinetic' the profile associated at the non-smooth velocity. In this case we give the minor (on the top) and major (on the bottom) scales.

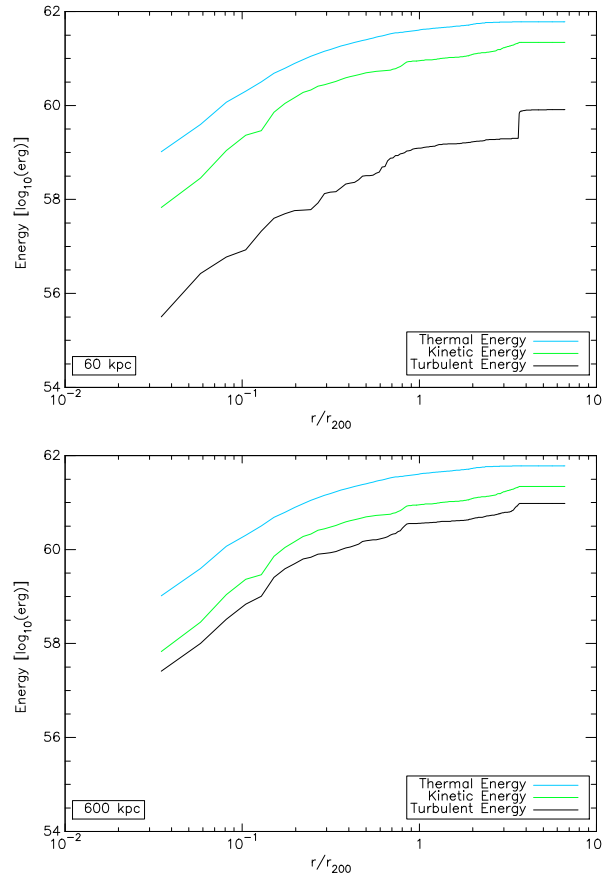


Figure 3.1: Cumulative profile of kinetic, turbulence and thermal energy for cluster IT90_3 at $z = 0$, considering two different smoothing scales (60 kpc on the top and 600 kpc on the bottom)

The effect of different scales is about two orders of magnitude in the center of the grid and about one order of magnitude in the periphery.

It is thus useful to present in this chapter the different fields that are used in our work. In the following figure we show three different maps: on the top left there is the unsmoothed velocity field, on the top right the smoothed ones, on the bottom the turbulence ones.

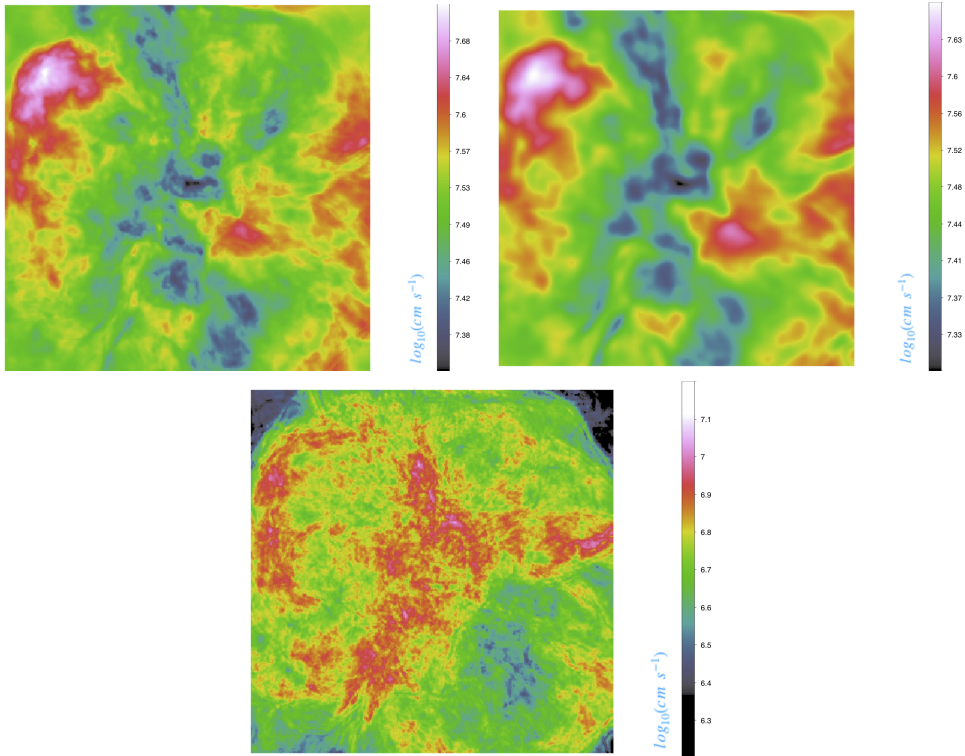


Figure 3.2: Maps of volume-weighted mean unsmoothed velocity field (on the top-left panel), smoothed velocity field (on the top-right panel) and turbulence velocity field (on bottom panel) for the cluster IT90_3 at $z = 0$.

We observe that the smoothing procedure filters the velocity field and results in a velocity field that we call 'turbulent'. From this field we will obtain the non-thermal pressure of the ICM that we will use throughout our analysis. However, it is necessary to apply a second type of filter which allows to exclude any spurious contributions to this turbulent velocity due to the shocks.

3.2 Limiting the spurious contribution from shocks to the turbulent budget

As discussed in section 2.2.2, the role of spurious terms introduced by shocks may affect the turbulence velocity field. In the following maps we present the turbulence velocity field before and after the application of our shock filtering algorithm (for a detailed explanation of our shock filtering procedure see next section).

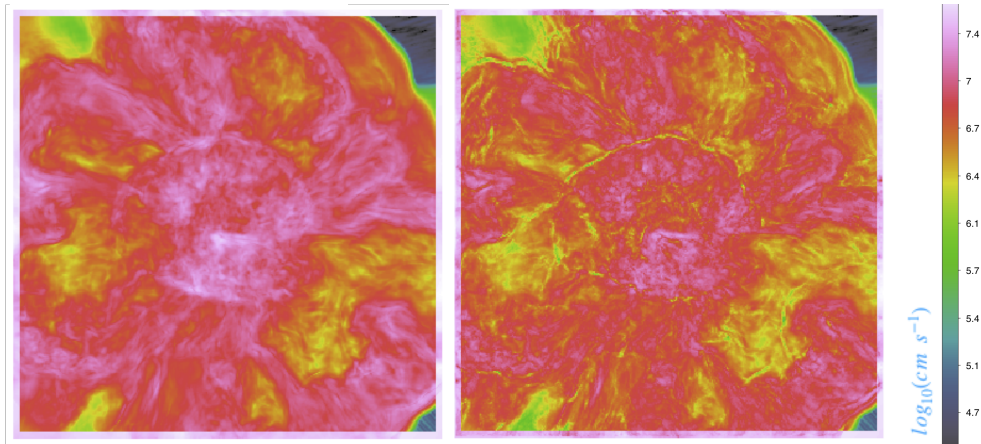


Figure 3.3: Map of central slice of IT90_3, turbulence velocity field without the application of shocks filter on the left panel and map of the same region with shocks filter on the right one.

In the figure 3.3 it is possible to see how the amount of turbulence velocity gets reduced in the region where shocks are detected.

In the following plots we give the profiles of turbulence velocity fields of all clusters, with and without the application of shocks filtering on the left panel and the median of these profiles on the right panel.

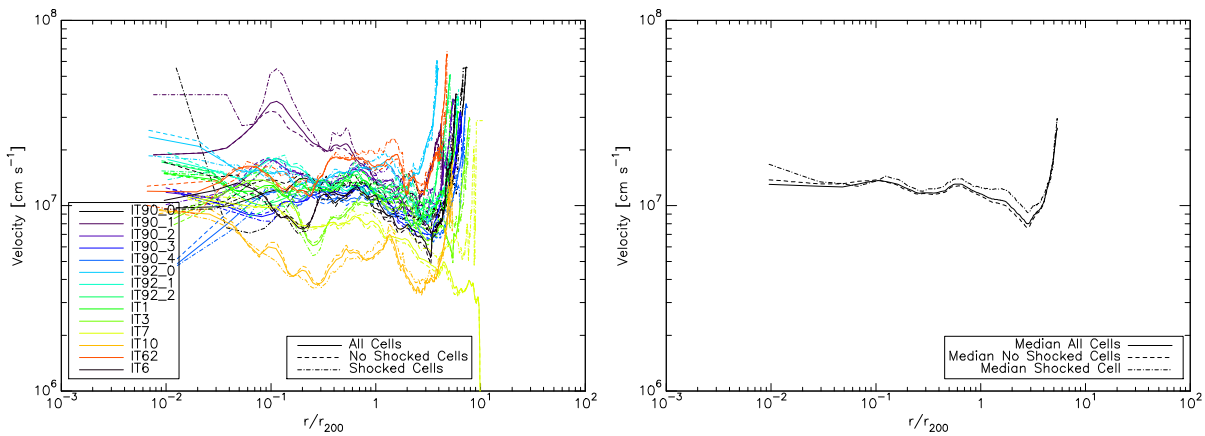


Figure 3.4: All turbulence velocity profiles for shock unfiltered velocity field and shock filtered velocity field (on the left panel) and median of the same profiles (on the right panel)

3.2.1 Shock Finder

In the study of turbulence, shocks crossing the simulated volume can introduce spurious terms in the estimate of turbulent kinetic energy (i.e. velocity jumps after shock crossing may be misled by small-scale velocity fluctuations due to turbulence). In order to avoid this bias we use the same shock finder algorithm presented in [Vazza et al. \(2017\)](#) with the goal of masking shocked cells from our analysis.

In the presence of shocks it is possible to use the Rankine-Hugoniot condition and use velocity or temperature jumps find the Mach number. The Mach number is used to calculate the flux of kinetic energy that is dissipated into gas thermal energy and this is the principal term that can affect our estimate of turbulent motions. The shock finder algorithm that we use follows the velocity jump prescription described in [Vazza et al. \(2009\)](#). In this paper the authors have shown that in order to compute the Mach number in post-processing, the velocity jumps are in general more suitable than temperature jumps, because in the latter case a typically larger amount of pre-shock temperature fluctuations in the intergalactic medium can affect the exact measurement of temperature jumps.

In the following there is a schematic work flow of the algorithm [Vazza et al. \(2009\)](#):

1. only cells with negative 3D velocity divergence are considered candidate shocked cells;
2. the center of the shocks region (typically few cells) is the cell with the minimum divergence velocity;
3. the three Cartesian axes are scanned with a 1D procedure measuring the velocity jump $\Delta v_{x,y,z}$ between a few cells across the shock center. In the case the shock is assumed to belong only to the cell $v_{x,y,z}$, the value of Δv is calculated between the shock center and the pre-shocked cell, while the shock jump is spread over few cells (placed at a maximum distance of $2n$), the value of Δv is calculated between the two cells at distance n (in opposite direction) from the center of the shock;
4. the Mach number of the shock is given by equation:

$$\Delta v = \frac{3}{4} v_s \frac{1 - \mathcal{M}^2}{\mathcal{M}^2} \quad (3.1)$$

where the sound speed is that of the pre-shock region;

5. we finally assign to shocked cells a Mach number

$$\mathcal{M}^2 = \sqrt{\mathcal{M}_x^2 + \mathcal{M}_y^2 + \mathcal{M}_z^2} \quad (3.2)$$

that minimizes projection effects in the case of diagonal shocks, and restrict the to shocks with $\mathcal{M} > 1$.

Detecting shocks with high Mach number is relatively easy with this algorithm, but the detection of shocks with small Mach number is affected by several factors like numerical error due to strong gradient or oblique direction of the shocks. In order to reduce the role of weak shocks in the following turbulence analysis, we decide to fix a lower limit to Mach number at 1.3.

In histogram 3.5 is clear how the shocks with low Mach number are more recurring than the shocks with high Mach number. From Mach number 1.3 to $\sim 10^3$, the number of cells interested by a shock drop by three order of magnitude.

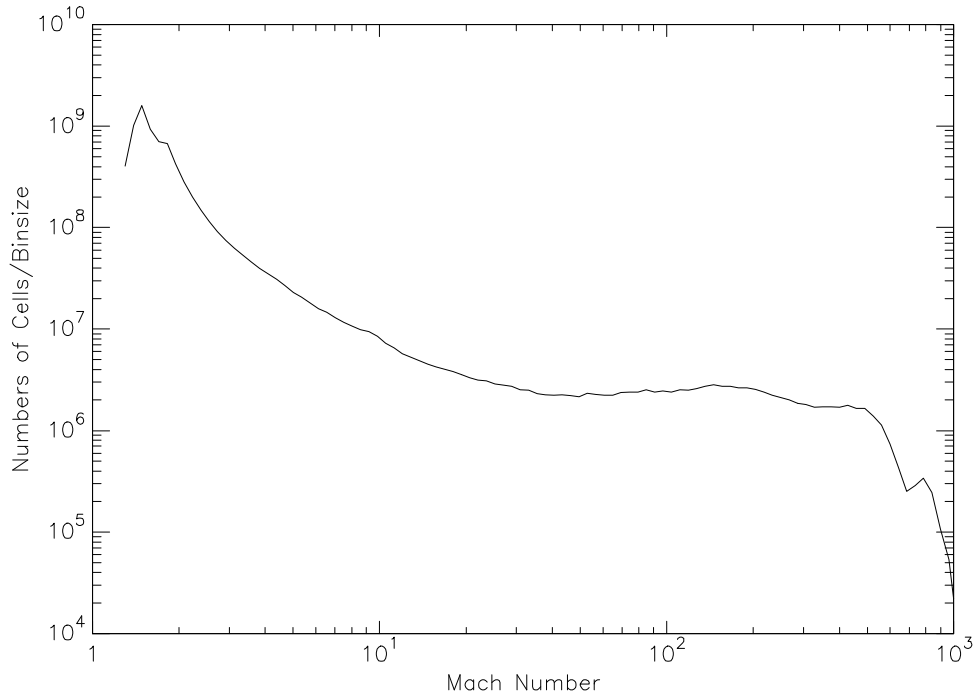


Figure 3.5: Mach number histogram of the shocks with $\mathcal{M} \geq 1.3$ in cluster IT90_3 $z = 0$.

In addition to the distribution presented in the histogram 3.5, we also show the spatial distribution of the shocks inside the cluster's volume. The following maps are projections of the distribution of Mach number and flux of energy dissipated by the shocks along an arbitrary line of sight, for the sake of simplicity choice in parallel to z-axis of the grid of the simulation.

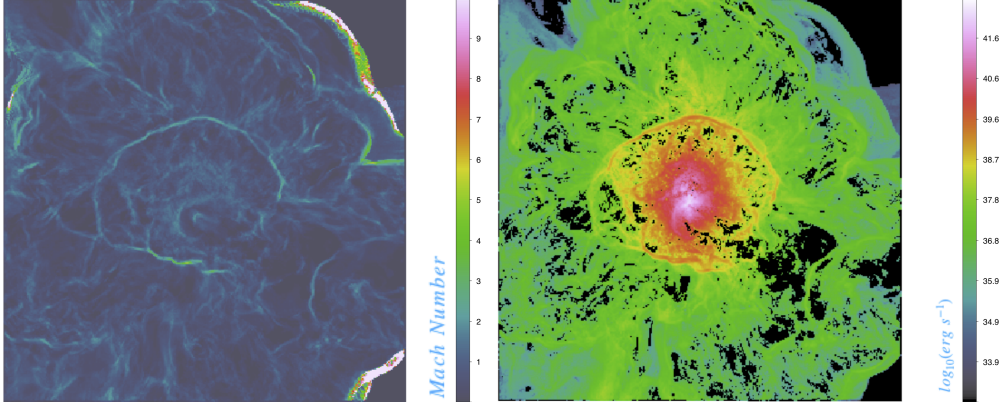


Figure 3.6: Map of central slice of IT90_3 at $z = 0$; map of projected Mach number (on the left panel) and map of projected flux of kinetic energy (on the right panel).

In figure 3.6, we note that in the center of the cluster only shocks with low Mach number are found, while in the outskirts shocks with a higher Mach number are possible. This effect occurs because in the periphery the gas temperature is smaller than in the center and the sound speed decreases. From equation 3.1, a larger sound speed entails a major velocity difference and hereupon Mach number increase. The map of flux of kinetic energy dissipated by shocks shows a more uniform behavior. This is due to the frequency of shocks sweeping the cluster volume. In fact, the gas mass processed by weak shocks is generally larger in the innermost cluster regions, hence the dissipated kinetic energy flux across internal shocks can be comparable (or larger) than the total dissipation in cluster outskirts, because the flow of kinetic energy through the shock is regulated by the equation:

$$f = \frac{\rho_{gas} V_{cell} v_s^3}{2t_s} = \frac{\rho_{gas}}{2} \cdot V_{cell}^{\frac{2}{3}} \cdot \mathcal{M}^3 \cdot \left(\frac{5k_b T}{3m_p} \right)^{\frac{3}{2}} \quad (3.3)$$

where $v_s = \mathcal{M}c_s$ is the shock velocity, $t_s = V_{cell}^{1/3}/v_s$ is the shock crossing time across the cell.

As presented at the beginning of this paragraph, it is therefore appropriate to consider the dissipation of kinetic energy by the shocks in order to correctly estimate the genuine turbulent budget of the intracluster medium and work out the hydrostatic mass bias in a robust way.

Chapter 4

Results and analysis

In this chapter we present all important results of our analysis. After a first presentation of the sample used, with particular attention to introduce the main techniques used and the physical parameters of the clusters, we give the results obtained for the analysis of the complete sample. In 4.4 section we discuss the results of the study of the two sub-samples. We divided our catalog in low and high mass compared to the average mass and relaxed and perturbed clusters compared to the average value of X-ray morphological parameters (see 4.1 for the definition of these parameters). In the last section we compare our results with two papers present in literature.

4.1 Cluster catalog

We used the "*Itasca Simulated Cluster*" sample (ISC) which is a set of 14 galaxy clusters in the $5 \cdot 10^{13} \leq M_{100}/M_{\odot} \leq 6 \cdot 10^{14}$ mass range (at $z=0$), simulated at uniform high spatial resolution ($\Delta x = 19.6$ kpc) with the Eulerian Adaptive Mesh Refinement and the Piecewise Parabolic method (PPM) in the *ENZO* code (Bryan et al., 2014). These simulations are non-radiative and assume the WMAP7 Λ CDM cosmology (Komatsu et al., 2011), with $\Omega_0=1.0$, $\Omega_B=0.0445$, $\Omega_{DM}=0.2265$, $\Omega_{\Lambda}=0.728$, Hubble parameter $h=0.702$, $\sigma_8=0.8$ and a primordial index of $n=0.961$. For each cluster are generated two levels of nested grids as initial conditions (each with 400^3 cells and dark matter particles and covering 63^3 [Mpc³] and 31.5^3 [Mpc³], respectively). At run time, two additional levels of *static* mesh refinement are imposed in the innermost 6.3^3 [Mpc³] volume around each cluster center, down to the $\Delta x=19.6$ [kpc/cell]. More information on the ISC sample can be found in Vazza et al. (2017) and Wittor et al. (2017).

Although the objects selected in this sample represent among the most massive objects in equivalent cosmic volume sampled by all runs, they do not define a mass-complete sample, which has some impact in the interpretation of some of our

results, as we shall see in the following sections.

In order to present the sample used in this work we shown the maps of projected density and the maps of temperature. The figure 4.1 shows the same line of sight for density and temperature projected maps. The clusters are sorted by the dynamical state from the most perturbed to the most relaxed (in the following section we discuss this division).

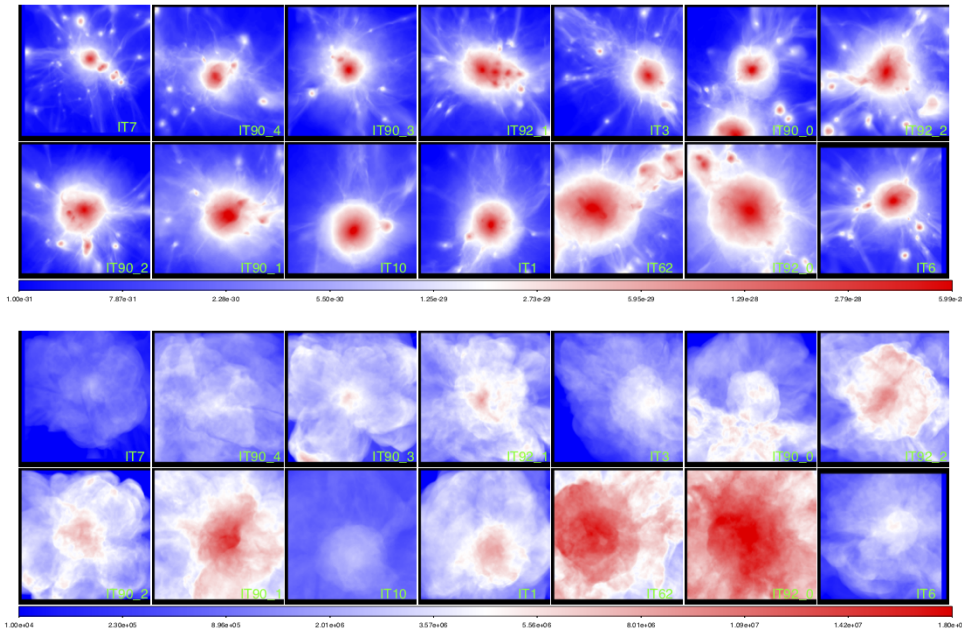


Figure 4.1: Density maps (on the top panel) and temperature maps (on the bottom panel) for all clusters used in this work (density color scale in unit of $[g\text{ cm}^{-3}]$ and temperature color scale in unit of Kelvin degrees)

The radial profiles of gas density and volume weighted temperature are given in Figure 4.2. For each system, we defined the center based on the maximum value of the total density (the sum of gas and dark matter density). All profiles are normalized to their value at R_{200} , which we measured where the value of total (gas + dark matter) density was greater than the value 200 of overdensity.

Furthermore, for each object we computed the total mass (M_{tot}), measured by the total density enclosed in R_{200} assuming spheroidal symmetry, the hydrostatic mass (M_{hyd}), measured from the equation 1.15, where the pressure is the thermal pressure of the gas, and the $\langle c \rangle$ and $\langle w \rangle$ morphological parameters of projected bolometric X-ray maps, made accessible by collaborators and computed as in Savini et al. (2018).

In detail, $\langle w \rangle$ is the emission centroid shift and $\langle c \rangle$ is the concentration parameter.

The first is defined as the standard deviation of the projected separation between the peak and centroid of the X-ray surface brightness distribution, when the aperture used to compute it decreases from a maximum radius of 500 kpc to smaller radii. $\langle c \rangle$ is defined as the ratio of the X-ray surface brightness within a radius of 100 kpc over X-ray surface brightness within a radius of 500 kpc. High values of w indicate a dynamically disturbed system, whilst high values of c indicate a peaked core, typical of non-merging systems.

We defined $\langle c \rangle$ and $\langle w \rangle$ because in simulations we have the 3D structure of the cluster, so we can compute the value of each parameter for any line of sight. We decided to use the projections parallel to the x, y and z axes and the final value for $\langle c \rangle$ and $\langle w \rangle$ is the mean of the three projected values.

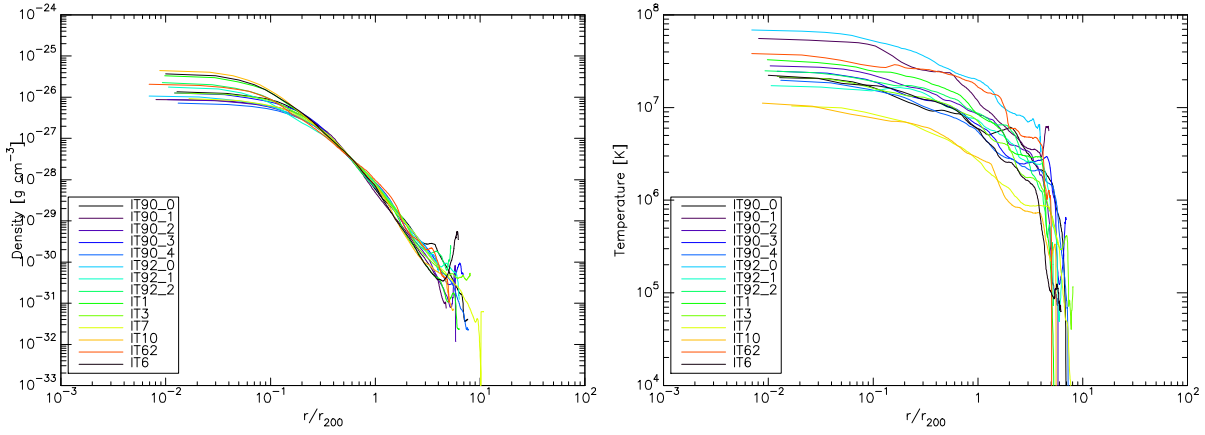


Figure 4.2: Density profiles (on the left panel) and temperature profiles (on the right panel)

All 14 clusters are used in our analysis and the table 4.1 shows the main properties of the clusters. In addition to identification name, mass and radius at overdensity 200 (called M_{200} and R_{200}) we report also the mass bias (i.e. total mass minus hydrostatic mass) and the total mass, parameters used to distinguish more or less massive clusters, and two parameters, $\langle c \rangle$ and $\langle w \rangle$, that they are used to distinguish between perturbed and relaxed clusters.

| ID | R_{200} [Mpc] | M_{200} [M_{\odot}] | $\frac{M_{tot,200}-M_{hyd,200}}{M_{200}}$ | $\langle c \rangle$ | $\langle w \rangle$ |
|--------|-----------------|---------------------------|---|--|--|
| IT90_0 | 0.80 | $5.73 \cdot 10^{13}$ | $-1.52 \cdot 10^{-1}$ | $7.48 \cdot 10^{-2}$ | $8.44 \cdot 10^{-3}$ |
| IT90_1 | 1.32 | $2.57 \cdot 10^{14}$ | $3.94 \cdot 10^{-2}$ | $2.72 \cdot 10^{-2}$ | $6.62 \cdot 10^{-3}$ |
| IT90_2 | 1.00 | $1.12 \cdot 10^{14}$ | $2.80 \cdot 10^{-1}$ | $4.45 \cdot 10^{-2}$ | $6.63 \cdot 10^{-3}$ |
| IT90_3 | 0.86 | $7.12 \cdot 10^{13}$ | $9.63 \cdot 10^{-2}$ | $6.81 \cdot 10^{-2}$ | $1.22 \cdot 10^{-2}$ |
| IT90_4 | 0.78 | $5.31 \cdot 10^{13}$ | $-1.82 \cdot 10^{-1}$ | $5.58 \cdot 10^{-2}$ | $1.27 \cdot 10^{-2}$ |
| IT92_0 | 1.46 | $3.48 \cdot 10^{14}$ | $1.55 \cdot 10^{-1}$ | $2.72 \cdot 10^{-2}$ | $3.84 \cdot 10^{-3}$ |
| IT92_1 | 0.96 | $9.90 \cdot 10^{13}$ | $1.25 \cdot 10^{-1}$ | $9.44 \cdot 10^{-2}$ | $1.13 \cdot 10^{-2}$ |
| IT92_2 | 1.10 | $1.49 \cdot 10^{14}$ | $4.34 \cdot 10^{-1}$ | $8.09 \cdot 10^{-2}$ | $6.67 \cdot 10^{-3}$ |
| IT1 | 1.04 | $1.26 \cdot 10^{14}$ | $1.02 \cdot 10^{-1}$ | $1.14 \cdot 10^{-1}$ | $5.65 \cdot 10^{-3}$ |
| IT3 | 0.84 | $6.63 \cdot 10^{13}$ | $-4.45 \cdot 10^{-1}$ | $8.47 \cdot 10^{-2}$ | $1.07 \cdot 10^{-2}$ |
| IT7 | 0.62 | $2.67 \cdot 10^{13}$ | $1.17 \cdot 10^{-1}$ | $1.06 \cdot 10^{-1}$ | $7.35 \cdot 10^{-3}$ |
| IT10 | 1.16 | $2.18 \cdot 10^{13}$ | $8.35 \cdot 10^{-2}$ | $1.21 \cdot 10^{-1}$ | $5.72 \cdot 10^{-3}$ |
| IT62 | 1.52 | $7.47 \cdot 10^{14}$ | $2.93 \cdot 10^{-1}$ | $5.19 \cdot 10^{-2}$ | $4.66 \cdot 10^{-3}$ |
| IT6 | 1.04 | $1.26 \cdot 10^{14}$ | $7.84 \cdot 10^{-2}$ | $1.27 \cdot 10^{-1}$ | $3.75 \cdot 10^{-3}$ |

Table 4.1: Catalog of clusters at $z = 0$ used in our analysis. The bold values are used to identify the perturbed clusters, based on the ranking of their $\langle c \rangle$ or $\langle w \rangle$ values, respectively.

For some clusters we observe that the value of the difference between total mass and hydrostatic mass versus total mass is negative. In the following analysis, in seeking the correlation between this quantity and other parameters, we use only the clusters that have their ratio positive.

We will use often data fitting with different models. In order to verify which model is better, we use the following definition of χ^2 , mathematical tool used in statistics which has different possible applications by varying its definition.

$$\chi^2 = \sum_{i=0}^N \frac{(data_i - model_i)^2}{\sigma_{data,i}^2} \quad (4.1)$$

where $\sigma_{data,i}$ is the value of data dispersion within each radial bin 'i'. In GDL's procedure, it is defined as the square root of the variance of data, that it is defined as ¹:

$$\sigma^2 = \frac{1}{N-1} \sum_{i=0}^{N-1} (x_i - \bar{x})^2 \quad (4.2)$$

¹When we obtain the parameters of best fit, we do not show the error associated at these value, because some of the outputs of the χ^2 procedure implemented in GDL resulted unreliable and potentially affected by bugs.

We define the non-thermal pressure P_{nt} and the thermal pressure P_{th} as:

$$P_{\text{nt}} = \frac{1}{3} \cdot \rho \cdot v_{\text{turb}}^2 \quad (4.3)$$

$$P_{\text{th}} = \frac{k_{\text{b}}}{\mu m_{\text{p}}} \cdot \rho \cdot T \quad (4.4)$$

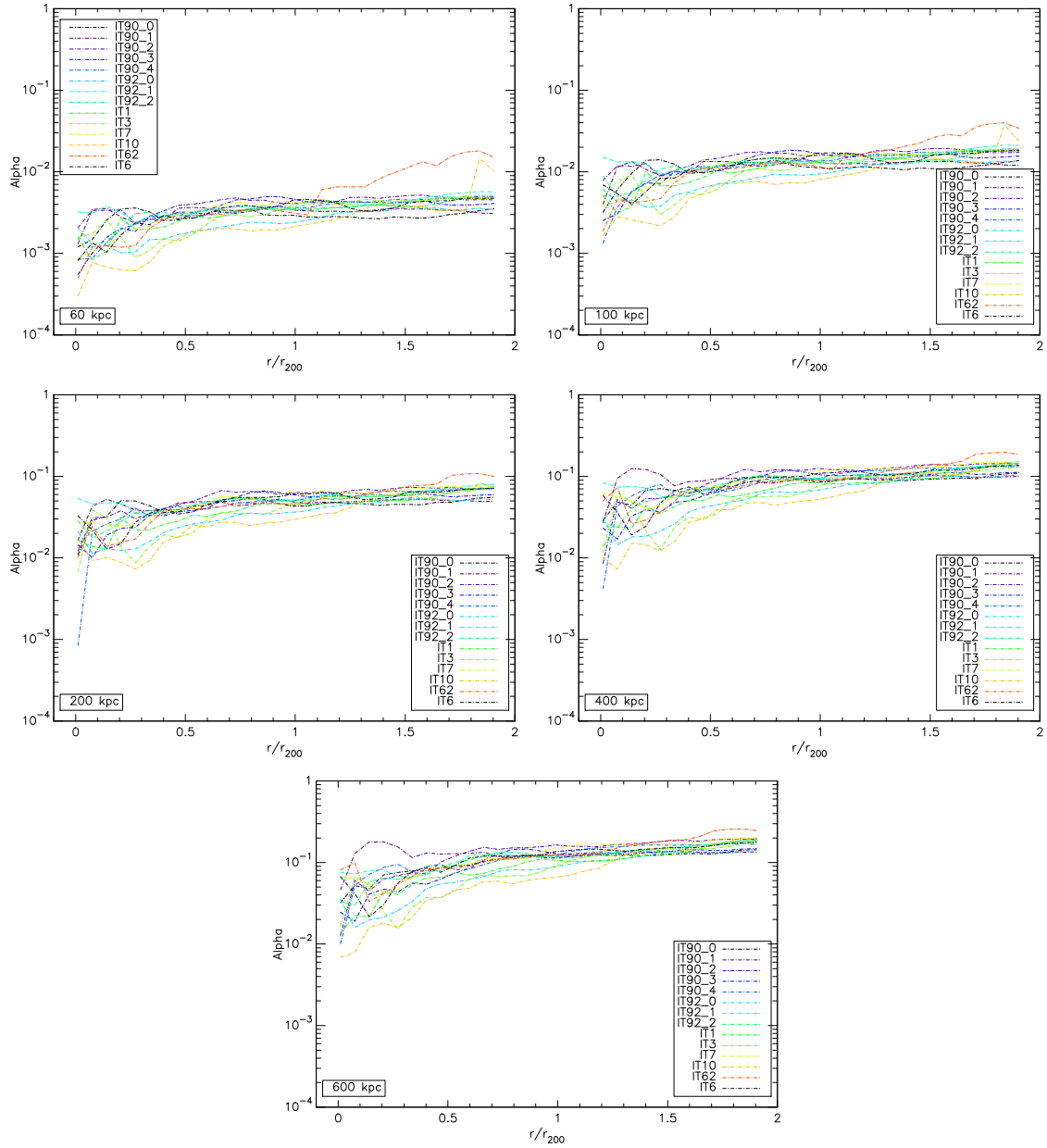
where ρ is the gas density, T is the gas temperature, k_{b} is the Boltzmann constant, m_{p} is the proton mass, μ is the mean molecular mass for electrons gas and its value is 0.59, v_{turb} is the turbulence velocity of the no shocked cells presented in the top panel of figure 3.4.

In order to study the ratio non thermal pressure versus total pressure (the sum of the non thermal and thermal pressure) we used the average radial profile of the pressures, always considering the same selection of cells. We call this ratio α and we defined it as follow:

$$\alpha \equiv \frac{P_{\text{nt}}}{P_{\text{nt}} + P_{\text{tot}}} \quad (4.5)$$

4.2 Complete sample analysis

In the figure 4.3 we show the profile of α for all the clusters as a function of smoothing scale. This ratio increases with the smoothing scale but for smoothing scales larger than few hundreds kilo-parsec the ratio approaches $\sim 10\%$ at R_{200} .

Figure 4.3: α radial profile for all clusters and for each smoothing scales

We compute the median of the profiles at single smoothing scale. The following figure shows all the median in the same plot.

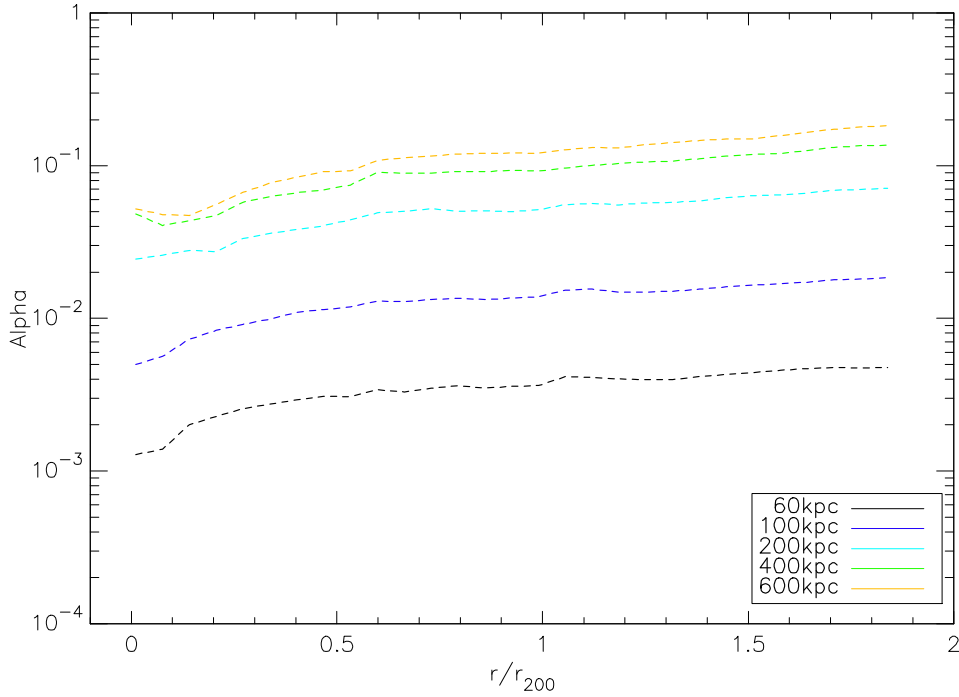


Figure 4.4: Median profiles for each smoothing scales

The profile is very regular at all scales and this it allows us to look for an analytical approximation to describe the behavior of α in function of radius. In order to find this approximation, we investigated the application of the following simple formula:

$$\alpha = a_0 \cdot \left(\frac{r}{r_{200}} \right)^{a_1} + a_2 \quad (4.6)$$

The parameters that we use in this equation are a_0 , a_1 and a_2 . a_0 represents the normalization of α at R_{200} and from the trend of the profiles we expect an increase of this value with the filtering scale.

The parameter a_1 is the slope of the profile and to give a physical explanation and a prediction about his behavior we refer to the paper of [Shi & Komatsu \(2014\)](#). In this paper the authors develop an analytic model to describe the trend of α with the radius. They use three fundamental time scales to develop their model: the turbulence dissipation time-scale, t_d ; the time elapsed between the initial time and the time of observation, $(t_{\text{obs}} - t_i)$, which characterizes the age of the cluster; and

a time-scale characterizing the mass growth rate of the cluster defined by t_{growth} . They defined also the turbulence injection efficiency η and which they constrained to $\eta \approx 0.5 - 1$ based on simulations. The turbulence injection efficiency is strongly correlated with the slope of the fitting formula, and we notice (as we shall see below) that our simulations suggest a lower efficiency than [Shi & Komatsu \(2014\)](#). Last parameter is a_2 that it represents the value of α at center of the cluster. In the center of clusters the turbulence is dominated by radiative cooling and AGN feedback (see sections 1.2 and 2.2.3), but they are not present in our simulations. It is however reasonable to expect small values of a_2 , because in the center of clusters there are chaotic motions of the gas connected with the dynamical history of the cluster.

The sum of a_0 and a_2 , which we defined as α_{200} , gives us the value of α at R_{200} . This parameter might be used in section 4.5 to compare our results with the results presented in [Eckert et al. \(2018\)](#). An other application that can be made with α_{200} is the study of a its possible relationship with the smoothing scale. With this study we investigate the process that controls the evolution of turbulence and we report our results later in this chapter.

We expect a strong dependence of the parameters by the smoothing scale, while the shape of the fits should be approximately independent of filtering. This behavior is regulated by Kolmogorov power spectrum, that it has the same slope for all the scales included from injection scale to the dissipation scale. The scales that we use for the smoothing of the velocity fields are included in this range and this explains why the slope of the fit of the individual scales should be approximately constant. The results of the fitting procedure, for all the smoothing scales, are given in the table 4.2.

| Smoothing Scale [kpc] | a_0 | a_1 | a_2 | χ^2 |
|-----------------------|-------|-------|--------|----------|
| 60 | 0.007 | 0.167 | -0.004 | 0.49 |
| 100 | 0.022 | 0.219 | -0.008 | 0.69 |
| 200 | 0.081 | 0.186 | -0.028 | 3.11 |
| 400 | 0.061 | 0.749 | 0.033 | 1.35 |
| 600 | 0.182 | 0.225 | -0.056 | 5.70 |

Table 4.2: Fitting parameters for our model

In the figure 4.5 we show the median profile and its fit for all the smoothing scales.

4.3 Relation between the filtering scale of turbulence and the non-thermal pressure support

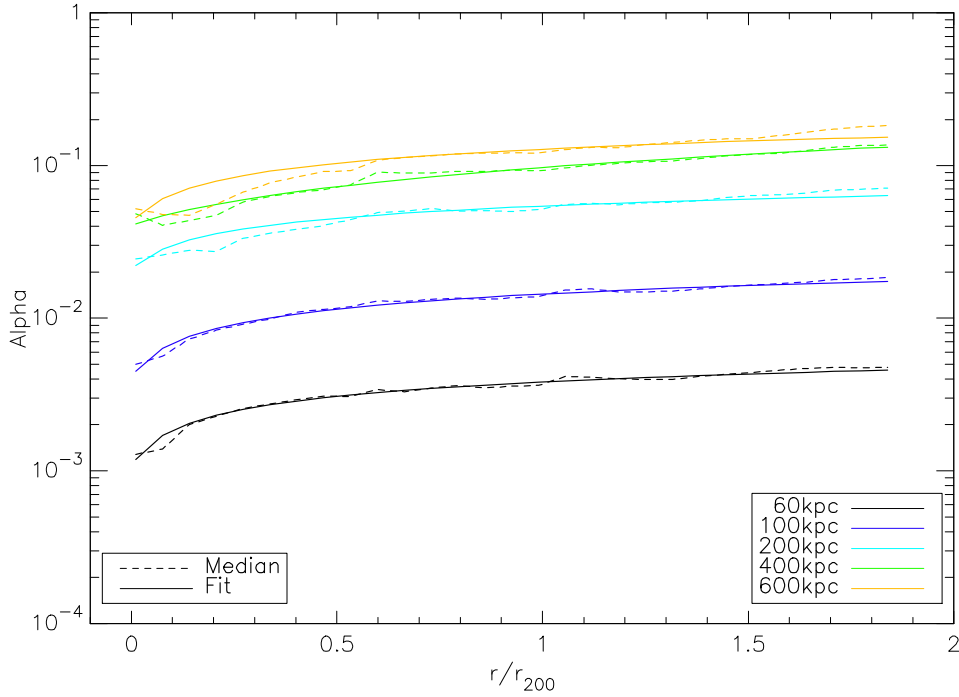


Figure 4.5: Median profiles and best fit relation for each smoothing scales

From both table 4.2 and figure 4.5 our fitting formula 4.6 well describes the data, yielding small χ^2 .

The parameters of the fits ensue the expectations described below. The terms that describe α in the center and at R_{200} increase with the smoothing scale, while the slope of fits is approximately the same for all the scales.

In section 4.5 we will compare our best fit formulas with other models proposed in the literature and we discuss which scale better describe the most recent observations.

4.3 Relation between the filtering scale of turbulence and the non-thermal pressure support

In order to test whether the standard Kolmogorv theory of turbulence (see section 2.1) applies to our data, we study the relation between the value of α_{200} and the smoothing scale. As shown in the previous paragraph, any smoothing scale generates different values of α_{200} . The smoothing scales can be associated at a different scales in Kolmogorov's spectrum. If we apply the "standard" relation between rms velocity and turbulent scale (e.g. $\sigma^2 \propto L^{\frac{2}{3}}$) in the stationary subsonic turbulent regime described by Kolmogorov theory, we expect that the relation is described

by the following function:

$$\alpha_{200} = a \cdot x^b \quad (4.7)$$

where 'x' is the value of smoothing scale in physical quantities and 'a' and 'b' are the parameters obtain from Kolmogorov's theory. The expected value for 'b', the slope of fit, is very close to $\frac{2}{3}$ in case the turbulence is stationary and subsonic, but ICM is not such an idealized environment (considering density stratification, self-gravity and un-stationary flow patterns), so the value expect for 'b' is relatively close to $\frac{2}{3}$ but not exactly this value. The figure 4.6 shows the relation α_{200} versus smoothing scale.

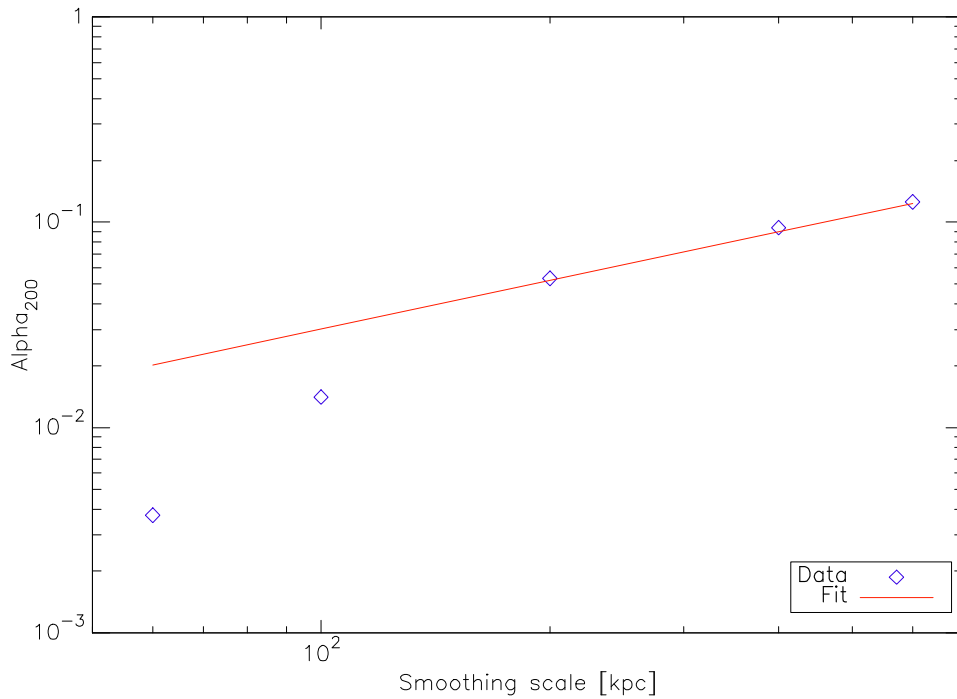


Figure 4.6: The symbols in the plot give the value of α parameter for the different smoothing scales, while the fit is obtain as described in the paragraph above

In order to find the value of parameters 'a' and 'b', we fit the data with the function 4.7 and we obtain:

- $a=8.00 \cdot 10^{-4}$
- $b=0.77$

The measured exponent $a_1 \cong 0.77$ is reasonably close to the $\frac{2}{3}$ exponent expected in Kolomogorov, and is consistent with the fact that the power spectra of

the velocity field in simulated galaxy cluster are typically steeper than the Kolmogorov's slope, because of the stratified cluster atmosphere, as presented in paragraph 2.1. Thus the scales 60 and 100 kpc are not well described by best fit relation. One sure reason for such steeper behavior at small scales is the effect of numerical dissipation, that is expected to artificially dampen velocity structures on scales close to the spatial resolution (e.g, Porter & Woodward 1994). If this scale is greater than the smoothing scale, the slope of Kolmogorov's spectrum is strongly steepened, as it is possible to observe in our plot. The typical scale for which this behavior is observable is ~ 8 times the resolution of the simulation. Our resolution is 20 kpc, so the scale for which the effect described in Porter & Woodward (1994) is observable is ~ 160 kpc. In figure 4.6 we note that the steepening of the spectrum occurs precisely by scales immediately below the 200 kpc scale. This suggests that for the scales below 200 kpc the value of α is strongly influenced by numerical effects. For scales greater than ~ 200 kpc these effects do not occur and the relation between α and the smoothing scale is well fitted by Kolmogorov's spectrum. Since a number of physical and numerical effects may affect the dynamics of the turbulent flow on <100 -200 kpc, with these simulations it is hard to tell the different effects apart, and in what follows we will mostly focus on the dynamics of the turbulence in the ICM on >100 kpc scales.

4.4 Sub-samples analysis

In order to study any possible dependence of α on the mass and on the dynamical state of the clusters, we have studied our sample after dividing it in high and low mass compared to median mass and relaxed or perturbed clusters compared to median of w or c parameters.

In this section we introduce a new smoothing scale. This scale is not at fix value like the previous ones, but its value is defined as $\frac{R_{200}}{3}$. Being so defined, this smoothing scale depends on the total mass of the single cluster and its value changes for each cluster. We have decided to use this scale to study possible relations between α and the type of filtering used to defined turbulence motions, as the maximum spatial scale of turbulent motions is likely connected to the cluster size (see ram pressure stripping section 2.2.1). From now, we will refer to this new scale calling it ' $\frac{R_{200}}{3}$ '. In the following section we show only the plot and we discuss the results for the two sub-samples. The tables like 4.2 that show the values of fitting parameters are showed in appendix B.

4.4.1 Mass division

From the table 4.1 we identify IT92_1 as the cluster with the median mass of our sample, so we divide our catalog in two sub-samples, that they are presented in the following table:

| | ID | | | | | | |
|-----------|--------|--------|--------|--------|--------|-----|--------|
| High Mass | IT62 | IT92_0 | IT90_1 | IT92_2 | IT1 | IT6 | IT90_2 |
| Low Mass | IT92_1 | IT90_3 | IT3 | IT90_0 | IT90_4 | IT7 | IT10 |

Table 4.3: Mass sub-samples

After defining the two sub-samples, we have separately analyzed the two groups, using the same technique used in section 4.2.

In the figure 4.7 we show the median profiles for the two sub-samples.

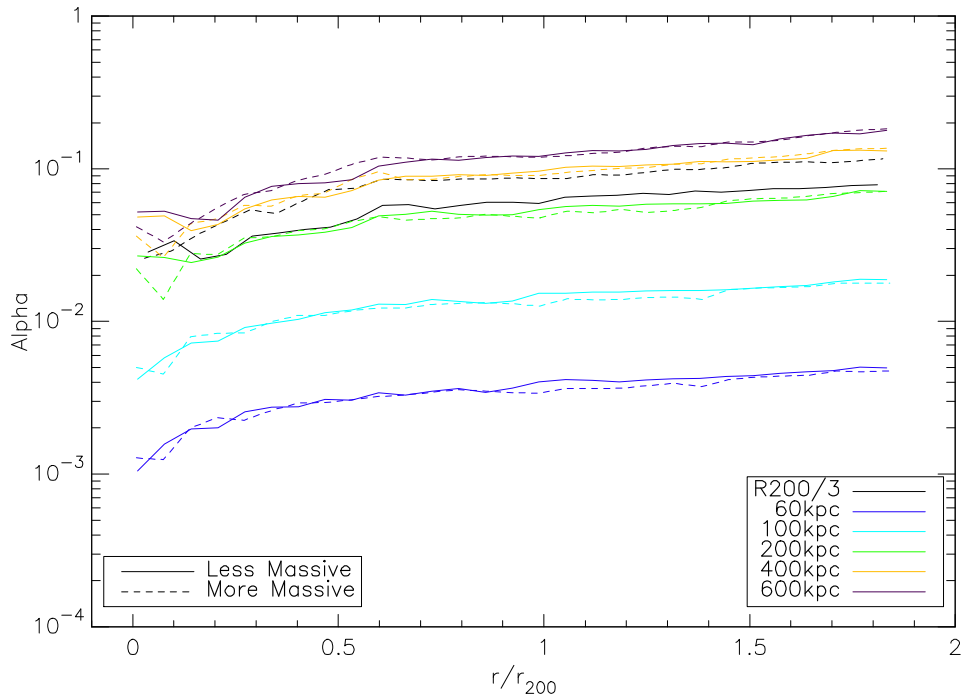


Figure 4.7: Median profiles for each smoothing scale and for high and low mass sub-samples

We apply the function 4.6 at the sub-samples, obtaining the fitting parameters reported in tables B.1 and B.2, and the following plots.

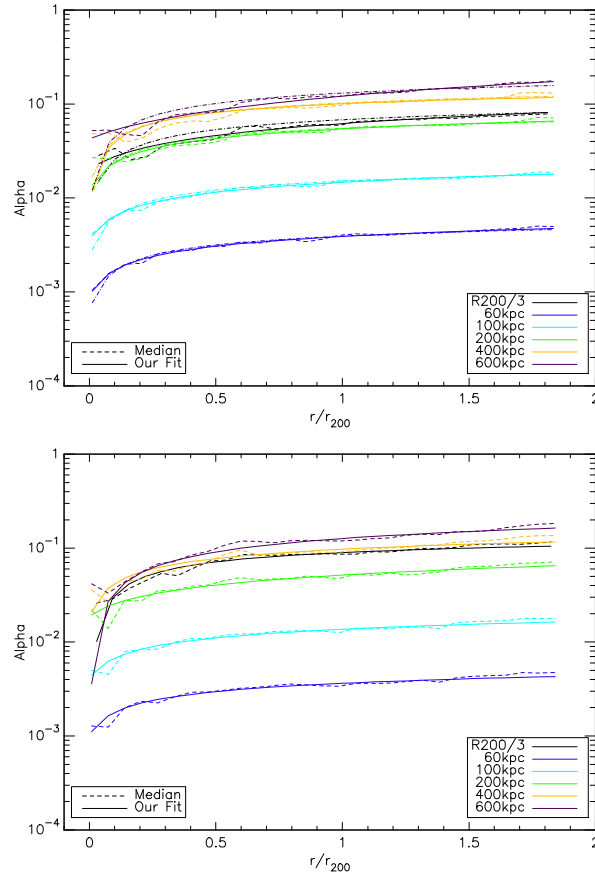


Figure 4.8: Less massive clusters (on the top panel) and more massive clusters (on the bottom panel) fitted for each smoothing scale

From figure 4.7, for fixed smoothing scales the difference between the two sub-samples is small, while for $\frac{R_{200}}{3}$ the difference is appreciable. Clusters with high mass are more perturbed than low mass ones. If we had a mass-complete sample this behavior could be explained by the fact that from the structure formation theory, we expect that more massive structure are formed at a later time than less massive ones. This suggests us that more massive clusters are far from virialization and they are more perturbed than the less massive clusters which have had time to virialize the ICM and we observe at them more relaxed.

However, we do not have a mass-complete sample so we can not entirely explain the behavior of the two sub-samples as presented below. However, we can explain this finding by analyzing the role that the filtering scale has on the final result. With fixed scales the larger eddies in more massive clusters are systematically filtered and the contribution of the bigger scales at the Kolmogorov's spectrum is lost. If we use a mass variable scale, which in our work is the same of using the $\frac{R_{200}}{3}$ scale,

we do not filter the bigger eddies in more massive clusters so their contribution at the computing of the turbulent pressure is not lost. This behavior is well shown in the figure 4.7 where the more massive clusters and the less massive ones have about the same shape for fixed smoothing scale, but for $\frac{\mathbb{R}_{200}}{3}$ scale the shapes are appreciably different.

In summary, from figure 4.8 we observe that our model well fit the two sub-samples, which is confirmed by the χ^2 reported in tables B.1 and B.2.

From all the evidence above described, it emerges that the mass division of the sample do not show strong evidence of dependence of turbulent pressure from the cluster's mass. This would be surprising if we used a mass-complete sample, for which we should observe more turbulent pressure in more massive clusters since they were formed last. Without a mass-complete sample, we can not give any constrains about mass-turbulent pressure relation, but we could still study relation between smoothing scales and α and the difference between the use of fixed smoothing scale or an adaptive mass scale.

4.4.2 Dynamic state division

In this section we investigated a possible relation between α and two X-ray morphological parameters often employed in the study of galaxy clusters to disentangle relaxed and perturbed clusters. We use the standard definitions for $\langle w \rangle$, the emission centroid shift, and $\langle c \rangle$, the concentration parameter (Mohr et al., 1993). In particular, the first is defined as the standard deviation of the projected separation between the peak and centroid of the X-ray surface brightness distribution, while the second is defined as the ratio of the X-ray surface brightness within a radius of 100 kpc over X-ray surface brightness within a radius of 500 kpc. Recalling that high values of w indicate a dynamically disturbed system, whilst high values of c indicate a relaxed cluster, now we present the results that we have obtained. The following tables show the two sub-samples used for the different parameters:

| | ID | | | | | | |
|-----------|--------|--------|--------|------|--------|--------|--------|
| Perturbed | IT92_0 | IT90_1 | IT90_2 | IT62 | IT90_4 | IT90_3 | IT90_0 |
| Relaxed | IT92_2 | IT3 | IT92_1 | IT7 | IT1 | IT10 | IT6 |

Table 4.4: $\langle c \rangle$ sub-samples

| | ID | | | | | | |
|-----------|--------|--------|--------|--------|------|--------|--------|
| Perturbed | IT7 | IT90_4 | IT90_3 | IT92_1 | IT3 | IT90_0 | IT92_2 |
| Relaxed | IT90_2 | IT90_1 | IT10 | IT1 | IT62 | IT92_0 | IT6 |

Table 4.5: $\langle w \rangle$ sub-samples

Before starting our analysis we notice that it is reasonable to expect a correlation between the cluster's mass and the dynamical state, because in a mass-complete sample the largest masses are associated to objects lately formed, which should be more turbulent on average. In the following plots we show the relations between mass and $\langle c \rangle$ or $\langle w \rangle$.

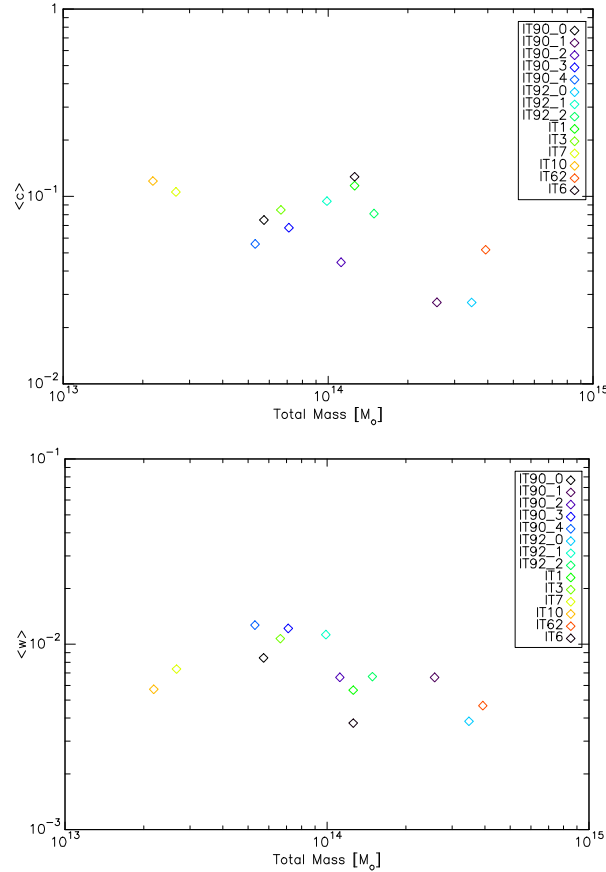


Figure 4.9: Mass- $\langle c \rangle$ relation (on the top panel) and mass- $\langle w \rangle$ relation (on the bottom panel) for each clusters

For $\langle c \rangle$ parameter we do not expect a strong trend of α with mass because this parameter is defined from quantities which are mostly determined by the dynamics in the central regions of the cluster only .

For $\langle w \rangle$ we expect that for fixed smoothing scale the α profiles for the two sub-samples (relaxed and perturbed) the difference are small, but for the $\frac{R_{200}}{3}$ scale the difference between the two sub-samples are appreciable. In particular, from the bottom panel of figure 4.9, we expect that for relaxed sub-sample α is for each radius greater than for perturbed sub-sample. This prediction comes from the fact

that less massive clusters have a value of $\langle w \rangle$ greater than more massive clusters. As discussed in section 4.1, high values of $\langle w \rangle$ identify perturbed clusters, so we expect that for $\frac{R_{200}}{3}$ scale, which separates the clusters in mass range, the value of α for perturbed clusters is smaller than for relaxed clusters. This behavior is therefore explained by a combination of effects due to the dynamic state but also by the relation between the mass and the filtering scale.

After this preliminary analysis, we focused on the individual parameters starting with $\langle c \rangle$ parameter. In the figure 4.10 are shown the median profiles of relaxed (identified with 'Relaxed') and perturbed (identified with 'Perturbed') clusters for each smoothing scales.

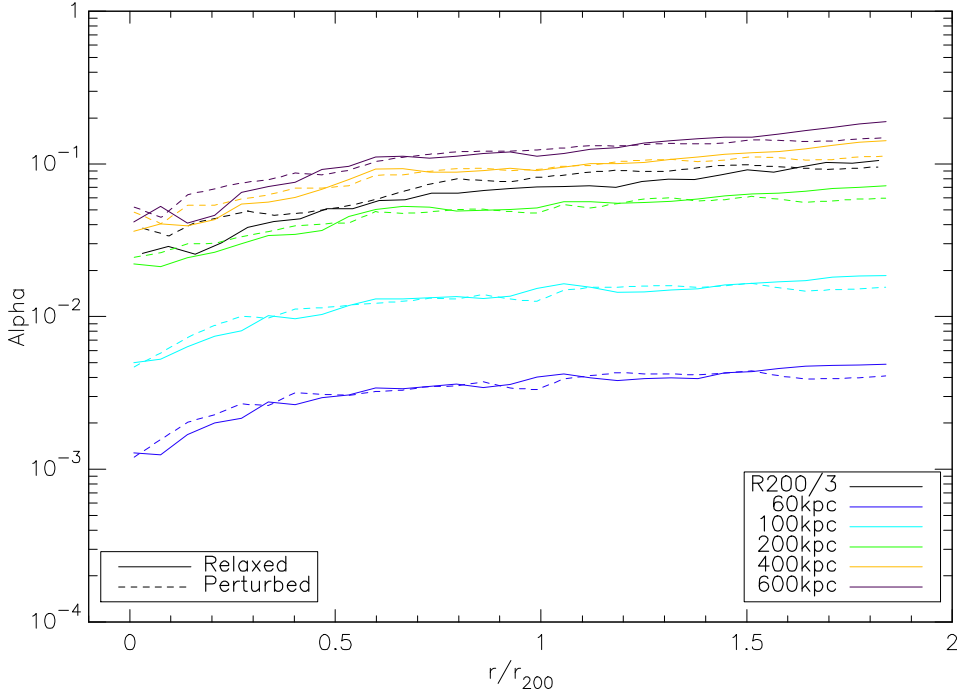


Figure 4.10: Median profiles for each smoothing scale and for perturbed and relaxed sub-samples for $\langle c \rangle$ parameter

For all the smoothing scales the difference between the two sub-samples is very small (≤ 2). The shape of the profile is similar to other samples used in our work, so we decide to fit these profiles with the same equation 4.6.

We observe also that in the core of the clusters, out to $\sim 0.4R_{200}$, the two samples have appreciable differences. Until $0.4R_{200}$ the perturbed sample has a larger α than the relaxed sample, for all smoothing scales. This behavior suggests that $\langle c \rangle$ parameter is a good indicator of turbulent motions only limited to the innermost regions of the cluster. Indeed, above $0.4R_{200}$ the shape of the perturbed and relaxed

samples is almost indistinguishable, which suggests the impossibility of using $\langle c \rangle$ as an indicator of turbulence outside of the cluster core. In the following plot we show the innermost region of the figure 4.10 where it is observed the behavior above described.

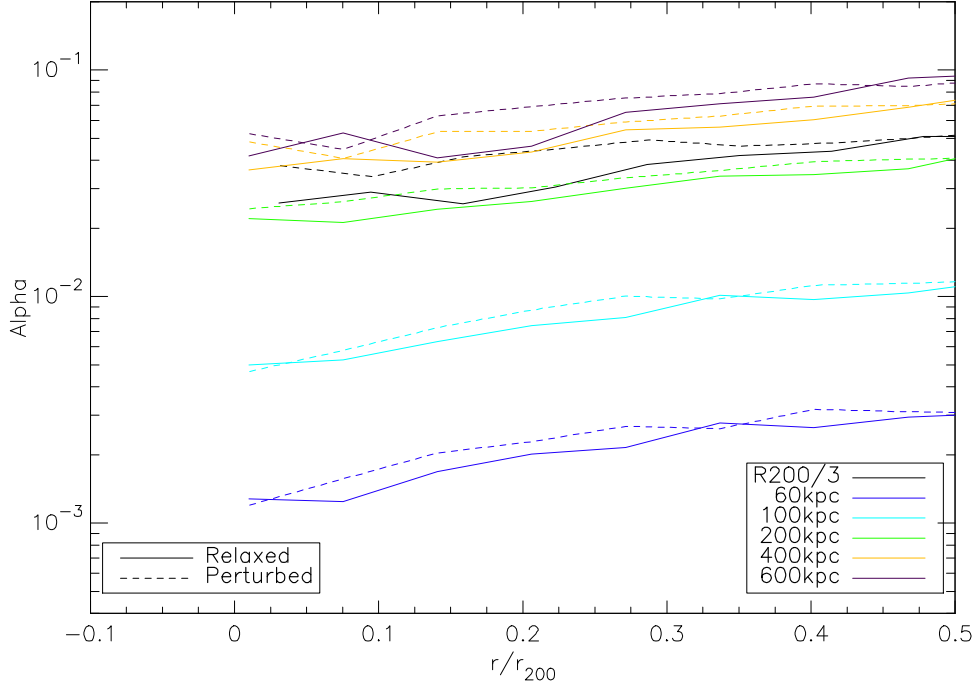


Figure 4.11: Median profiles for each smoothing scale and for perturbed and relaxed sub-samples for $\langle c \rangle$ parameter, zoomed in the region $0 < r < 0.4R_{200}$

From the tables B.3 and B.4, we observe that our fitting formula well described the profiles and for perturbed clusters the χ^2 is smaller than for relaxed ones, for all the smoothing scales.

In order to study a possible correlation between α_{200} and value of $\langle c \rangle$ for each clusters, we derived the values of α_{200} as described in section 4.2. We study also the correlation between α in the core of the clusters and $\langle c \rangle$ parameter. We obtain the results shown in the following figure:

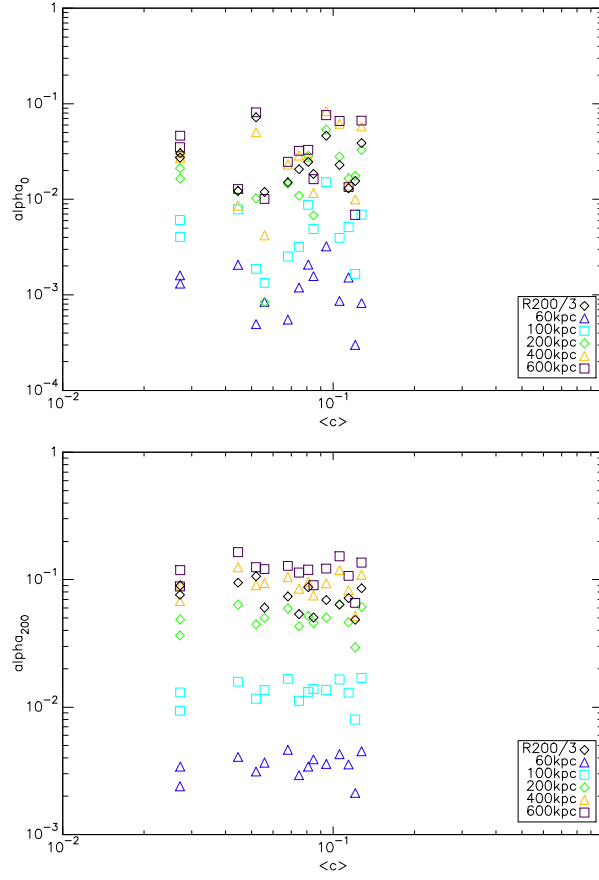


Figure 4.12: Comparison between α in the core and $\langle c \rangle$ parameter for each cluster (on the top panel) and comparison between α_{200} and $\langle c \rangle$ parameter for each cluster (on the bottom panel).

From the distribution of the data is not possible identify a correlation between α_{200} and $\langle c \rangle$. This means that it is not possible use the parameter $\langle c \rangle$ as a indicator of turbulence in ICM above $0.4R_{200}$. We remark that, even if a slightly more evident correlation between $\langle c \rangle$ and α may be present limited to the innermost $\leq 0.4R_{200}$ region, the scatter in our data is still to large to allow any firm conclusion (see right panel of figure 4.12).

In order to verify if this behavior is due to real nature of ICM or it is due to the fact that $\langle c \rangle$ is not the best indicator for this type of study, we have decide to apply the same technique at $\langle w \rangle$ parameter.

We show in the figure 4.13 the median for relaxed and perturbed clusters with the same nomenclature adopted for the analysis of $\langle c \rangle$ parameter.

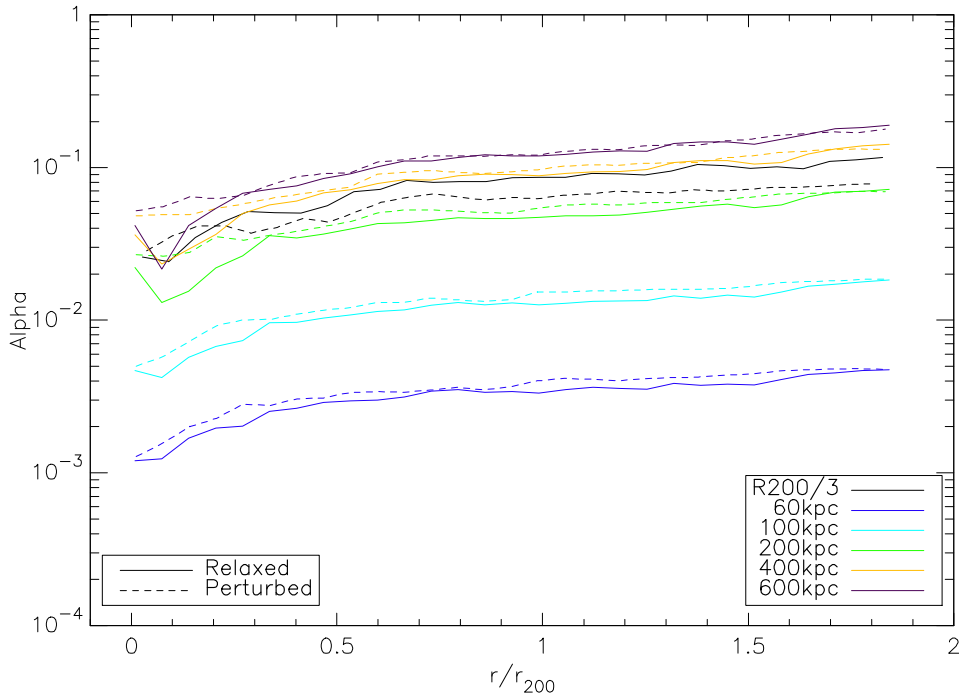


Figure 4.13: Median profiles for each smoothing scale and for high and low mass sub-samples for $\langle w \rangle$ parameter

As discussed at the begin of this section, we note that for fixed filtering scale the difference between the two sub-samples is negligible, but for the $\frac{R_{200}}{3}$ scale this difference gets significant. Our prediction turns out to be correct and the explanation we gave seems to be correct.

As for $\langle c \rangle$ analysis, we apply the function 4.6 at two samples separately and from tables B.5 and B.6 we observe that our function well fits the data, with a behavior similar to $\langle c \rangle$ parameter. Comparing statistically $\langle w \rangle$ and $\langle c \rangle$, the results of fitting procedure of $\langle w \rangle$ sample is slightly less accurate than the $\langle c \rangle$ one.

It is important to study the correlation between $\langle w \rangle$ and α_{200} , in order to verify whether the parameters normally used to identify relaxed and perturbed clusters could be used also to identify the clusters more turbulent.

In Figure 4.14 we show the result of correlation between $\langle w \rangle$ and α_{200} .

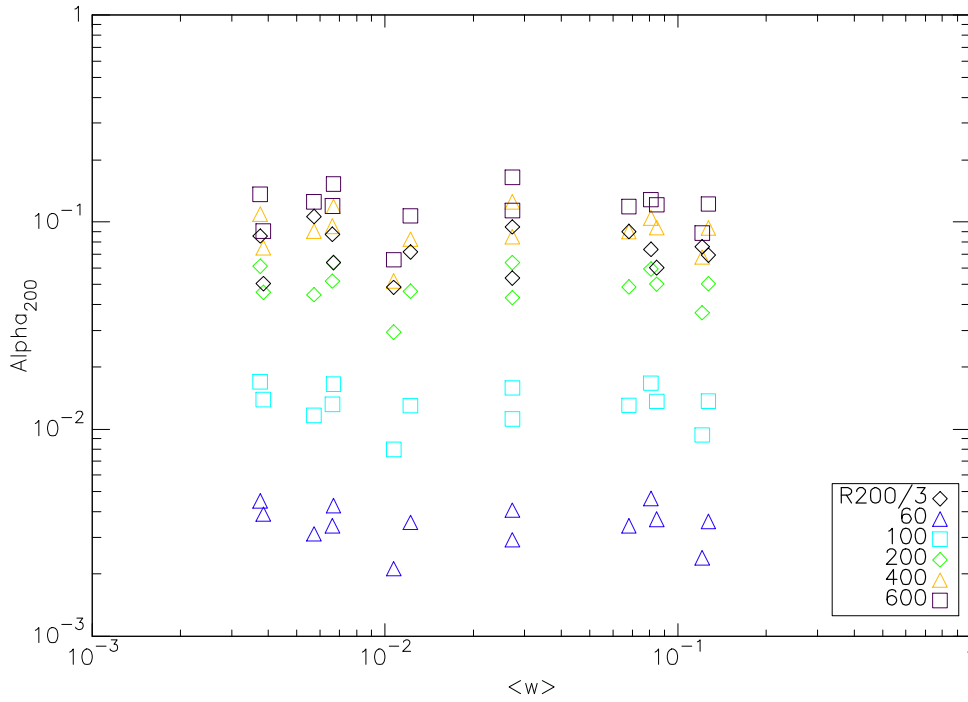


Figure 4.14: Comparison between α_{200} and $\langle w \rangle$ parameter for each cluster

As the case of $\langle c \rangle$ parameter it is not possible to identify a strong correlation between the two parameters, but in this case a weak correlation is observable.

From our analysis, it emerges that $\langle c \rangle$ is not a reliable indicator of turbulent pressure at radii greater than $0.4R_{200}$. It is however a weak indicator of turbulence motions in the core of the cluster only. This is interesting for the future X-ray space telescope missions as Athena, for which the resolution of observation will be such as to be able to study in depth the core of the clusters.

For $\langle w \rangle$ we conclude that it is a weak but reliable indicator of turbulent pressure at R_{200} . In particular, its relation with the cluster's mass and its relatively easy determination, makes it a good indirect indicator of turbulence motions in the outskirts of the cluster.

In conclusion, from the analysis of the two parameters $\langle w \rangle$ and $\langle c \rangle$ does we report no strong correlation between dynamical state of clusters and their turbulent motions. This goes against our expectations and it makes necessary a more in-depth study of all the possible sources of correlations between dynamic state and turbulent motions, including the impact of not having a mass-complete sample of galaxy clusters. In the chapter 5 we discuss a possible approach a these studies and some expectations of their results.

4.5 Comparison with recent literature

After the analysis presented above, we compare our work with the recent literature. In particular, we compare our results with a theoretical work published in [Nelson et al. \(2014\)](#) and an observational work published by [Eckert et al. \(2018\)](#).

In [Nelson et al. \(2014\)](#), the authors used a sample of 65 cosmological clusters simulated in cosmology, using the Adaptive Refinement Tree N-body+gas-dynamics code ART. The clusters are selected with successive mass-cut, fixing different mass for different redshift. This sample was analyzed in order to estimate the non-thermal pressure support from gas motions as a function of radius.

The difference between our work and the work of [Nelson et al. \(2014\)](#) is the filtering procedure of velocity field. They followed the procedure presented in [Zhuravleva et al. \(2013\)](#). For each radial bin they excluded the contribution from gas in the high-density tail in the gas distribution, with the goal of removing small-scale fluctuations in the non-thermal pressure due to gas substructures while preserving the profiles of the global ICM. In addition, they smoothed the profiles and then they computed the mean $\langle v_i \rangle$ and mean-square gas velocities $\langle v_i^2 \rangle$ weighted by the mass of each gas cell. The velocity dispersion is computed as $\sigma_i = \sqrt{\langle v_i^2 \rangle - \langle v_i \rangle^2}$, distinguishing between radial and tangential velocity components, σ_r and σ_t . The 3D velocity dispersion is computed as $\sigma_{gas} = \sqrt{\frac{\sigma_r^2 + \sigma_t^2}{3}}$.

For their samples, the authors find that the following fitting formula best describes their data:

$$\frac{P_{rand}}{P_{total}}(r) = 1 - A \left\{ 1 + \exp \left[- \left(\frac{r}{B} \right)^\gamma \right] \right\} \quad (4.8)$$

with $A=0.452 \pm 0.001$, $B=0.841 \pm 0.008$ and $\gamma=1.628 \pm 0.019$.

In order to verify which method gives statistically better results, we apply the fitting formula 4.8 to our clusters and we obtain the parameters shown in the following table:

| Smoothing Scale [kpc] | A | B | γ | χ^2 |
|---|------|------|----------------------|----------|
| 60 | 0.73 | 0.43 | $3.97 \cdot 10^{-3}$ | 0.61 |
| 100 | 0.73 | 0.41 | $1.56 \cdot 10^{-2}$ | 0.93 |
| 200 | 0.70 | 0.34 | $6.14 \cdot 10^{-2}$ | 3.28 |
| 400 | 0.69 | 0.24 | 0.13 | 5.18 |
| 600 | 0.68 | 0.27 | 0.19 | 5.25 |
| in Nelson et al. (2014) paper | 0.45 | 0.84 | 1.63 | |

Table 4.6: Fitting parameters for Nelson model

Table 4.6 must be compared with table 4.2 and the following figure compares our model and the Nelson model.

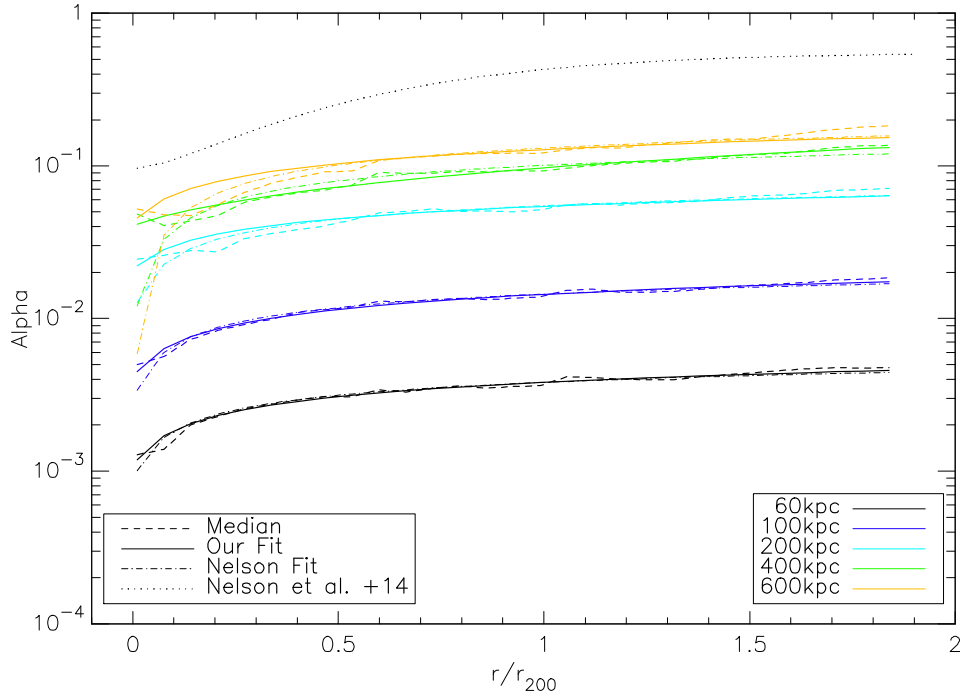


Figure 4.15: Comparison between our model and the model proposed by Nelson et al. (2014)

From the comparison between the tables 4.6 and 4.2 we can conclude that our model describes better the data, or is substantially comparable with Nelson model at most filtering scales. From figure 4.15 it is possible to observe that the shape of the best fit is about the same for both the fitting formula. This suggests that the formula suggested by Nelson is flexible enough to equally accommodate the fitting of our data. However, the advantage of our proposed best fit formula is that the free parameters have a simple physical meaning (see section 4.2). On the other hand, if we directly compare with the best fit parameters suggested in Nelson et al. (2014), we find that the function 4.8 with the parameters proposed in there (in plot above dotted line) is not able to describe the data in any smoothing scales.

The differences between our results and the results presented in Nelson et al. (2014) are attributable to the different choice in filtering velocity fields because there the authors apply a type of filter which considers the turbulent velocity as the contribution of radial motions and tangential motions. This assumption tends to overestimate the real turbulent velocity field, as presented in Vazza et al. (2018). As presented in this paper, the amount of turbulent pressure is overestimated by a fac-

tor 2-3 when radial motion are left unfiltered. In our work we use a filter that is more conservative and is more suitable to yield the isotropic pressure support from turbulent gas motions. Furthermore, in this work we also apply a shock filter which allow us to exclude the spurious contributions of shocks. The importance of this filter is discussed in section 3.2. These considerations let us believe that our filtering procedure is likely better compared to the procedure used in Nelson et al. (2014). In particular, our definition of kinetic pressure is more realistic because we consider this pressure as an isotropic pressure.

To verify if our procedure can also better describe the observed data, we compare our results with a recent observational work (Eckert et al., 2018). In this paper the authors study the turbulence in ICM on a sample of 12 clusters observed in X-ray band using the space telescope XMM-Newton. In particular the authors focus their study at two radius, R_{500} and R_{200} . The authors compared the hydrostatic mass that can be derived up to R_{200} using SZ data from the Planck satellite, with the total mass that can be derived up to the same radius based on the observed X-ray emission profile, which is converted into a total mass under the assumption (supported by simulations) that the baryon fraction in clusters approaches its cosmic value at $\sim R_{200}$. From the mis-match between the two estimates of the total mass, it is thus possible to derive the non-thermal pressure bias. Following Eckert et al. (2018), in the presence of isotropic non-thermal pressure, the hydrostatic equilibrium equation can be generalized as:

$$\frac{d}{dr}(P_{th}(r) + P_{NT}(r)) = -\rho_{gas} \frac{GM_{tot}(< r)}{r^2} \quad (4.9)$$

with P_{th} and P_{NT} the thermal and non-thermal pressure components, respectively. They set the non-thermal pressure fraction as $\alpha(r) = \frac{P_{NT}(r)}{P_{tot}(r)}$ and the equation above can be rewritten as:

$$M_{tot}(< r) = M_{hyd}(< r) + \alpha(r)M_{tot}(< r) - \frac{P_{th}r^2}{(1-\alpha)\rho_{gas}G} \frac{d\alpha}{dr} \quad (4.10)$$

from which we get α as:

$$\alpha = 1 - \frac{\rho_{gas}GM_{hyd} + \sqrt{(\rho_{gas}GM_{hyd})^2 - 4M_{tot}\rho_{gas}GP_{th}R^2\frac{d\alpha}{dr}}}{2M_{tot}\rho_{gas}G} \quad (4.11)$$

Therefore, from the observed bias between the hydrostatic mass and the total mass it is indeed possible to estimate the value of non-thermal pressure in the outer regions of galaxy clusters, and this is the same quantity that we can independently derive from our simulations.

We investigate now the possibility of the most appropriate smoothing scales of filtering that best reproduce the data derived by Eckert et al. (2018), by benchmarking the outcome of the different scales against the results based on recent XMM observations. In figure 4.16 we show the median profiles at each smoothing scales and the results of α for the clusters of paper Eckert et al. (2018).

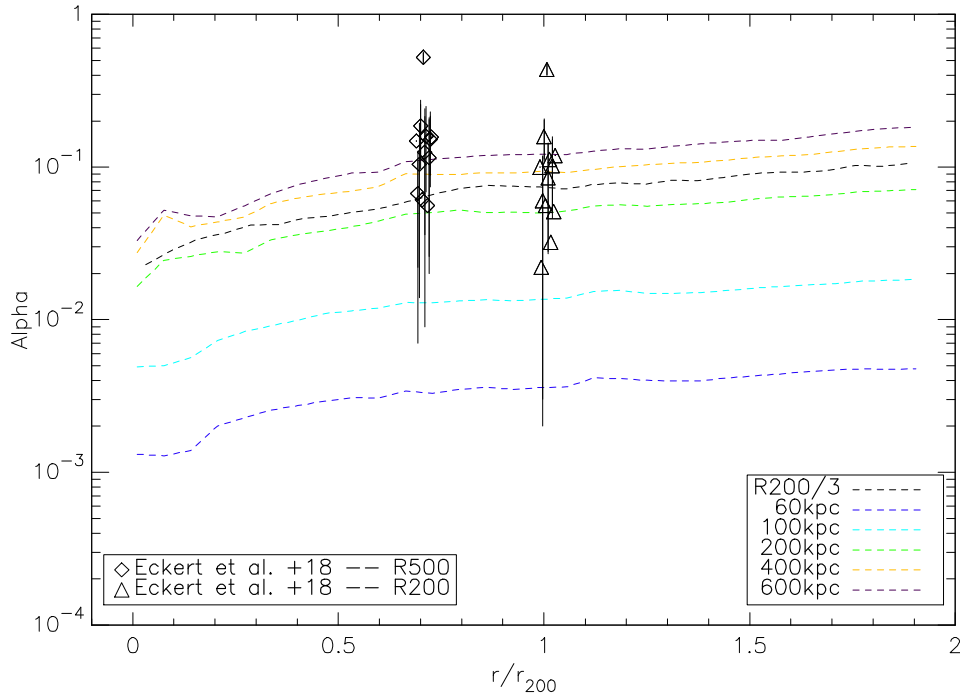


Figure 4.16: Comparison between our α median profiles for each smoothing scale and the observed data points by Eckert et al. (2018)

While the smaller scales (60 and 100 kpc) do not explain well the data of Eckert et al. (2018), the scales from 200 to 600 kpc fit the data in a good way. This is reasonable, because the scales from 200 to 600 kpc are the scales at which the turbulence is injected in ICM. These are the typical scales of the ram pressure stripping and the clumps which are observed in X-ray maps. Also the choice of a scale that depends on the cluster radius (i.e. $\frac{R_{200}}{3}$ in figure 4.16) well matches the observations. Based on these observations and from what we discussed in the previous sections, we can conclude that the scale $\frac{R_{200}}{3}$ is probably the best one to filter the velocity fields and therefore this may be the best guess for the typical outer scale of turbulent motions in the ICM, implied by our work.

Chapter 5

Conclusions and future perspectives

In this chapter we summarize the main results of our work, we discuss the main sources of uncertainty and we present what our future perspectives may be.

Methods and data

We have analyzed a recent high-resolution sample of galaxy clusters, simulated with the cosmological code *ENZO*, specifically designed to study turbulent motions in the ICM.

We optimized existing algorithms to disentangle laminar from bulk motions in the simulated ICM, and we developed new tools to limit the spurious contribution from gas clumps and shocks in the simulated volume.

We therefore produced the 3-dimensional distribution of turbulence in simulated clusters at $z=0$, which represents the starting point of our analysis. From this distribution we defined the turbulent velocity field and we compute the non-thermal contribution of pressure.

We computed the 3-d profiles of non-thermal and thermal pressure. For the thermal support we used the simulations data of temperature, while for the non-thermal one we used the turbulent velocity which is obtained from the filtering above described. Then we defined the ratio of non-thermal pressure versus the total pressure (non-thermal and thermal contribution) as α and we computed the radial profile of this quantities for each cluster.

From the profiles of each clusters, we further built the average profile across our sample, by re-normalizing and fixing the radial length in order to have a comparable distribution for each cluster.

In order to study possible correlations between turbulent pressure and mass or dy-

namical state of the cluster, we further divided our dataset into sub-samples. In particular, we computed the mass of the each cluster and we divided our sample in low and high mass compared to the median mass. Furthermore, we could divide our sample in relaxed and perturbed clusters using the dynamical state, which is defined by two different morphological X-ray parameter 'w' and 'c'. In particular we used the mean of the two parameters along three different line of sight and we indicate these parameters as $\langle w \rangle$ and $\langle c \rangle$. $\langle w \rangle$ is the emission centroid shift and $\langle c \rangle$ is the concentration parameter. The first is defined as the standard deviation of the projected separation between the peak and centroid of the X-ray surface brightness distribution, when the aperture used to compute it decreases from a maximum radius of 500 kpc to smaller radii. $\langle c \rangle$ is defined as the ratio of the X-ray surface brightness within a radius of 100 kpc over X-ray surface brightness within a radius of 500 kpc. High values of w indicate a dynamically disturbed system, whilst high values of c indicate a peaked core, typical of non-merging systems.

Results

Our work has produced several results that can be summarized in this section. Part of these results have also been crucial for a peer-reviewed article, [Vazza et al. \(2018\)](#) which I coauthored.

We developed a new fitting formula for the radial profile of α in the form:

$$\alpha = a_0 \cdot \left(\frac{r}{r_{200}} \right)^{a_1} + a_2$$

This formula well fits the data of our simulations, both for complete sample and for the different sub-samples which we studied. We found that the three parameters can be easily related to the physics of the ICM (see section 4.2 for a detailed explanation and the necessary bibliographic references).

Our results imply that on average the ratio between non-thermal to total pressure, supplied by gas turbulence, is over $\sim 0.5\%$ at R_{200} considering velocity scales < 60 kpc, and $\sim 10\%$ within the same radius, considering velocity scales from 400 to 600 kpc. The pressure ratio in the very center of clusters is on average $\sim 0.1\%$ and $\sim 5\%$, respectively.

We study the relation between the value of α at R_{200} and the value of smoothing scale, finding that the trend expected from the Kolmogorov theory well fits our data only for the largest smoothing scales (~ 200 -600 kpc). This is likely due to the fact that the ICM in the simulations is stratified and there are many numerical effects that change the slope of the spectrum.

We compare our results with the results presented in [Nelson et al. \(2014\)](#). We notice that the main different between the two approaches is in the definitions of

turbulent velocity. We applied a shock filter and a smoothing procedure to the velocity, while in [Nelson et al. \(2014\)](#) the authors defined the turbulent velocity from the radial motions of the gas. Our results overall suggest that our definition of turbulent velocity is more accurate than the definition used in [Nelson et al. \(2014\)](#). In particular we refer a recent work by [Vazza et al. \(2018\)](#) where the authors demonstrate that the definition which is used by [Nelson et al. \(2014\)](#) overestimated the turbulent pressure by a factor 2 or 3.

We also compare our results with a recent observational work by [Eckert et al. \(2018\)](#). In this paper the authors use a sample of observed X-ray clusters and they measured the non-thermal pressure at two radii, R_{500} and R_{200} . We have shown in [4.5](#) that the smoothing scales from 200 to 600 kpc well fit the observational data and it suggest us that our definition of turbulent motions is sufficiently correct to explain observational features. The comparison with observational data suggests us that the best scale that described the turbulent motions is in the range between 200 and 600 kpc, so we focused our study in this range.

Thanks to all the previous conclusions, we found that a practical approach to best extract the turbulent kinetic energy in cluster outskirts is to filter out motions with a coherence scale larger than $\sim \frac{R_{200}}{3}$, where R_{200} is the cluster's radius. With this choice, we can automatically account for the change in the outer injection scale of clusters with different masses, owing at the fact that smaller clusters typically accrete smaller substructures compared to larger objects, following self-similarity. This scale allowed us to study particular features as the relation between α , X-ray morphological parameters and the cluster's mass (see the section [4.4.2](#)).

Thanks to the dynamical state division we can conclude that the c parameter is a weak indicator of turbulence only in the innermost region of the cluster (typically inner to $0.4R_{200}$) while in the outskirts it is not possible use c as an indicator of turbulence. However, the w parameter is a weak but good indicator of turbulence in the outskirt region of the cluster. In particular, for the w parameter we found a possible relation between $\langle w \rangle$ and the mass of the cluster, when we smooth the velocity field with a mass sensible scale (in our analysis $\frac{R_{200}}{3}$ scale).

Present limitations

From the conclusions presented above we notice that there are some important physical and numerical issues that we have to consider in our analysis. In particular we can summarize them in:

- Limited numerical resolution: the resolution of the simulation which is used in this work is 20 kpc. The main effect is already discuss and may lead to an underestimate of non-thermal pressure at scales which are less than ~ 8 times the numerical resolution ([Porter & Woodward, 1994](#));

- **Statistical completeness:** our sample was not designed to be complete in mass, hence it is difficult to clearly identify physical effects that depends on the total size of the host cluster and not on its internal dynamics;
- **Physical issues:** a number of additional physical effects (from radiative gas cooling to AGN feedback) can indeed increase the level of turbulence, at least within cluster cores. Based on [Vazza et al. \(2013\)](#), however, we expect these effects not to be relevant for the estimate of the turbulent pressure support in cluster outskirts and on >200 kpc scales, which is our main focus here.

In addition to numerical and physical issues we notice that also the sample that we use in this work may introduce some biases. In particular we can summarize these effects in:

- **Incomplete-mass sample:** this may affect the conclusions derived from the analysis of the mass division and dynamical state division of the sample. In particular we found that there is little to no correlation between the mass of the clusters and the non-thermal support, but also there are not correlations between dynamical state and the non-thermal pressure. This is contrary to our expectations as already discuss in the sections [4.4.1](#) and [4.4.2](#). This likely stems from the fact that the sample that we have select to this work is not a mass complete sample, so we can not draw firm conclusions;
- **No massive clusters in the sample:** the sample which we use lacks of clusters with value of total mass higher than $7.5 \cdot 10^{14}$. This could be affect the conclusions of our work, because we expect that more massive clusters are formed in later time compared to the less massive ones. Moreover, the most massive clusters are also the one for which more observational results are available. From these different formation times we expect that more massive clusters are also more perturbed and they are characterized by more turbulent motions, while less massive clusters are more relaxed and their non-thermal support is less than more massive clusters. However, this behavior is not observed in our sample and we relate this to the fact that in our sample there are no clusters with high mass and the mass range is not so extend as to allow us to see these evolutionary effects.

Future developments

After presenting the results and the main issues of our work, we conclude this chapter with some possible future perspectives that we think are interest upgrade

of this work. Some of the above issues could be addressed by using a larger, mass-complete sample. In particular with an other type of selection we may be able to observe the typical behavior expect from the structure formation theory, like the fact that more massive clusters are more perturbed and turbulent than the less massive ones. From the simulations we used in this work, we can access many time steps of the individual clusters. If we consider separate time steps of at least one dynamic scale time, we will be able to the same cluster at several different times as two separate clusters. This would allow us to increase our statistics and have a mass-complete sample.

Different definition of X-ray parameters: for the dynamical state division we use the typical X-ray definition of c and w parameters and we considered the mean value of three line of sight. These definitions are often used in observational works, but in numerical work we can use many line of sight and we can define the dynamical state of the cluster as the mean of more line of sight. We think that the mean of the parameters which is calculated from many line of sight, it could be enclose the information necessary to find the relationships between dynamical state and non-thermal support.

In conclusion, this work was born as an analysis of the turbulence in the ICM gas, but it has opened the possibility of new studies on the relationships that link the turbulent pressure to the dynamic state of the cluster and its mass. The origin of the problems we have discussed in our work are not fully constrained, but with future and more focused work on specific details, we will be able to better constrain the linke between the turbulent pressure support in cluster outskirts also as a function of cluster's mass and dynamical state.

Appendix A

Numerical algorithm

In this appendix we presented the numerical algorithms which we used and developed for our analysis. The main parts which need a more detailed explanation are presented in the section 3. Here we summarize the main steps that we followed to obtain our results.

With gray color in scheme A.1 we show all the inputs used in different part of the code. In particular we report the fields from simulations (density, temperature and velocity), the shock finder algorithm (see Vazza et al., 2017, for details), the procedures used to compute the mass and other physical quantities of each cluster, the estimate of X-ray morphological parameters, which are computed by collaborators, and the procedure used to normalized the radial profile of α .

As result of the procedure which we developed, we obtain radial profiles of α and a catalog, with mass, virial radius and X-ray parameters, which in the scheme are colored in yellow.

With these results we produced the analysis of different samples. In particular begun with the complete sample, from which we obtained the new fitting formula described in section 4.2. After this first analysis, we divided our sample in more massive clusters and less massive ones, compared to the median mass. After the mass division, we also divided our sample in perturbed and relaxed clusters, using two different X-ray morphological parameters, $\langle c \rangle$ and $\langle w \rangle$. In the scheme A.1 these division are shown in green.

The results obtained with the algorithm above are the data products that we used to investigate the physical properties of the ICM and to further compare with the literature. This final analysis part is showed in the bottom of the scheme and it is colored in blue.

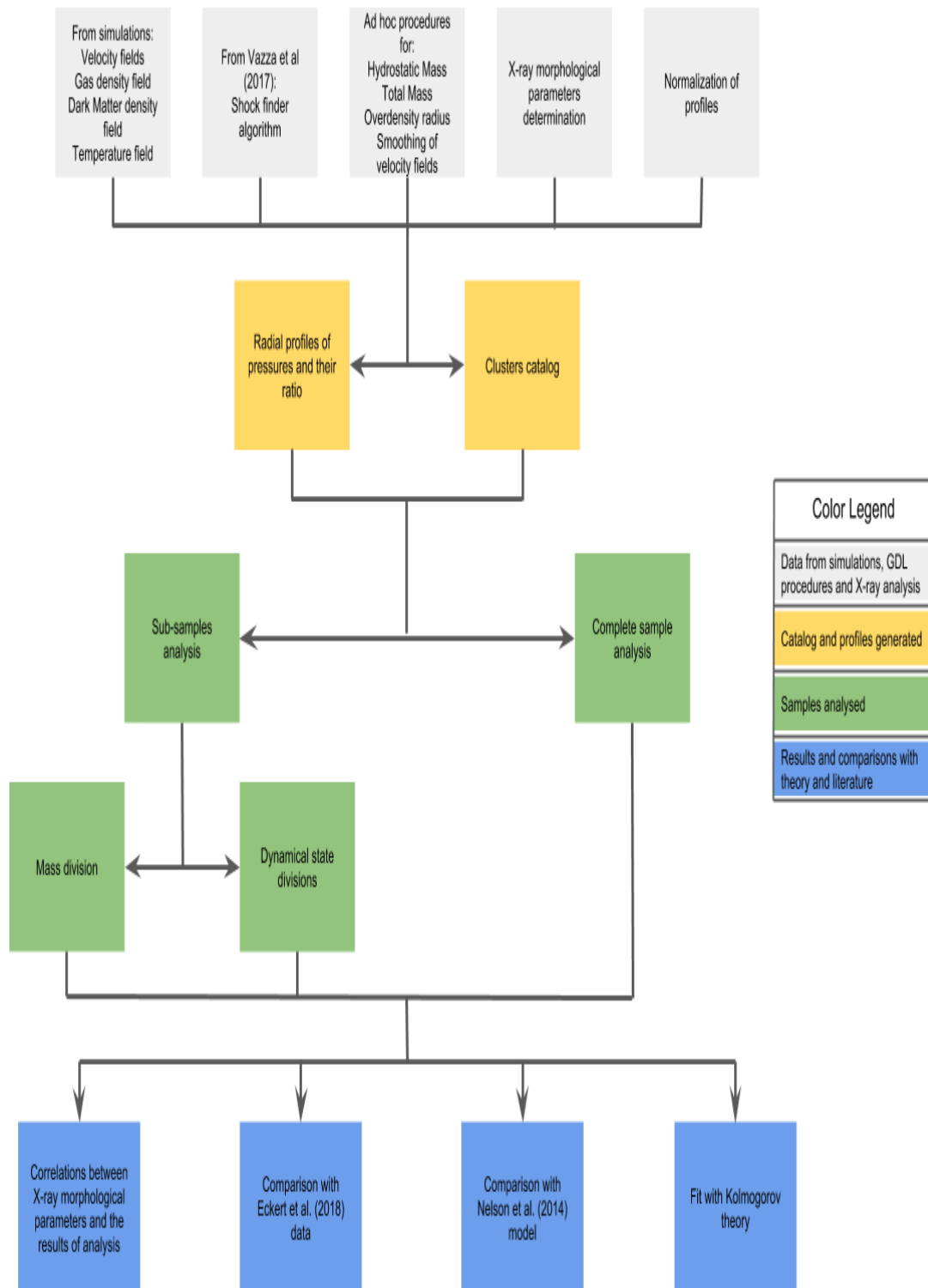


Figure A.1: Schematic work-flow

Appendix B

Fitting parameters for sub-samples

In this appendix we shown the table of best fit parameters for each sub-samples used in our analysis. The fitting formula used is:

$$\alpha = a_0 \cdot \left(\frac{r}{r_{200}} \right)^{a_1} + a_2 \quad (\text{B.1})$$

In particular the tables [B.1](#) and [B.2](#) refer to the results obtained for more massive sub-samples and less massive sub-samples, which are presented in section [4.4.1](#). The tables [B.3](#) and [B.4](#) refer to perturbed and relaxed sub-samples obtained from the $\langle c \rangle$ parameter division, while [B.5](#) and [B.6](#) refer to perturbed and relaxed samples obtained from $\langle w \rangle$ parameter division. The dynamical state division is described in section [4.4.2](#).

The physical meaning of the parameters A_0 , A_1 and A_2 is the same presented in section [4.2](#), while the χ^2 is described in section [4.1](#).

| Smoothing Scale [kpc] | A_0 | A_1 | A_2 | χ^2 |
|-----------------------|-----------------------|-----------------------|-----------------------|----------|
| 60 | $9.84 \cdot 10^{-3}$ | $1.11 \cdot 10^{-1}$ | $-6.27 \cdot 10^{-3}$ | 0.73 |
| 100 | $2.40 \cdot 10^{-2}$ | $1.73 \cdot 10^{-1}$ | $-1.14 \cdot 10^{-2}$ | 1.16 |
| 200 | $4.63 \cdot 10^{-2}$ | $4.24 \cdot 10^{-1}$ | $4.05 \cdot 10^{-3}$ | 2.78 |
| 400 | $3.65 \cdot 10^{-1}$ | $8.79 \cdot 10^{-2}$ | $-2.69 \cdot 10^{-1}$ | 3.88 |
| 600 | $2.93 \cdot 10^{-1}$ | $2.01 \cdot 10^{-1}$ | $-1.70 \cdot 10^{-1}$ | 3.16 |
| $\frac{R_{200}}{3}$ | $-2.16 \cdot 10^{-1}$ | $-1.29 \cdot 10^{-1}$ | $3.04 \cdot 10^{-1}$ | 2.27 |

Table B.1: Fitting parameters for high mass sample

| Smoothing Scale [kpc] | A_0 | A_1 | A_2 | χ^2 |
|-----------------------|-----------------------|-----------------------|-----------------------|----------|
| 60 | $7.38 \cdot 10^{-3}$ | $1.85 \cdot 10^{-1}$ | $-3.57 \cdot 10^{-3}$ | 0.49 |
| 100 | $2.40 \cdot 10^{-2}$ | $2.21 \cdot 10^{-1}$ | $-9.66 \cdot 10^{-3}$ | 0.63 |
| 200 | $1.23 \cdot 10^{-1}$ | $1.52 \cdot 10^{-1}$ | $-6.94 \cdot 10^{-2}$ | 2.93 |
| 400 | $-3.19 \cdot 10^{-1}$ | $-9.41 \cdot 10^{-2}$ | $4.18 \cdot 10^{-1}$ | 7.51 |
| 600 | $8.38 \cdot 10^{-2}$ | $8.01 \cdot 10^{-1}$ | $3.30 \cdot 10^{-2}$ | 2.00 |
| $\frac{R_{200}}{3}$ | $5.18 \cdot 10^{-2}$ | $5.45 \cdot 10^{-1}$ | $8.32 \cdot 10^{-3}$ | 2.14 |

Table B.2: Fitting parameters for low mass sample

| Smoothing Scale [kpc] | A_0 | A_1 | A_2 | χ^2 |
|-----------------------|----------------------|----------------------|-----------------------|----------|
| 60 | $2.89 \cdot 10^{-3}$ | $3.75 \cdot 10^{-1}$ | $8.02 \cdot 10^{-4}$ | 2.06 |
| 100 | $3.14 \cdot 10^{-2}$ | $1.42 \cdot 10^{-1}$ | $-1.74 \cdot 10^{-2}$ | 1.16 |
| 200 | $5.26 \cdot 10^{-2}$ | $3.21 \cdot 10^{-1}$ | $-1.98 \cdot 10^{-3}$ | 1.33 |
| 400 | $3.37 \cdot 10^{-1}$ | $8.77 \cdot 10^{-2}$ | $-2.44 \cdot 10^{-1}$ | 1.55 |
| 600 | $1.22 \cdot 10^{-1}$ | $3.84 \cdot 10^{-1}$ | $-2.20 \cdot 10^{-3}$ | 0.84 |
| $\frac{R_{200}}{3}$ | $5.61 \cdot 10^{-2}$ | $7.38 \cdot 10^{-1}$ | $2.14 \cdot 10^{-2}$ | 1.47 |

Table B.3: Fitting parameters for perturbed clusters selected by $\langle c \rangle$ parameter

| Smoothing Scale [kpc] | A_0 | A_1 | A_2 | χ^2 |
|-----------------------|----------------------|----------------------|--------------------------|----------|
| 60 | $5.03 \cdot 10^{-3}$ | $2.71 \cdot 10^{-1}$ | $-1.38 \cdot 10^{-3}$ | 2.85 |
| 100 | $1.68 \cdot 10^{-2}$ | $3.16 \cdot 10^{-1}$ | $-3.05 \cdot 10^{-3}$ | 3.28 |
| 200 | $3.85 \cdot 10^{-2}$ | $6.31 \cdot 10^{-1}$ | $1.24 \cdot 10^{-2}$ | 3.19 |
| 400 | $1.22 \cdot 10^{-1}$ | $4.16 \cdot 10^{-1}$ | $4 - 2.52 \cdot 10^{-2}$ | 5.77 |
| 600 | $9.14 \cdot 10^{-2}$ | $8.43 \cdot 10^{-1}$ | $2.45 \cdot 10^{-2}$ | 4.49 |
| $\frac{R_{200}}{3}$ | $5.10 \cdot 10^{-2}$ | $7.86 \cdot 10^{-1}$ | $1.58 \cdot 10^{-2}$ | 1.44 |

Table B.4: Fitting parameters for relaxed clusters selected by $\langle c \rangle$ parameter

| Smoothing Scale [kpc] | A_0 | A_1 | A_2 | χ^2 |
|-----------------------|----------------------|----------------------|-----------------------|----------|
| 60 | $7.16 \cdot 10^{-3}$ | $1.78 \cdot 10^{-1}$ | $-3.30 \cdot 10^{-3}$ | 0.94 |
| 100 | $2.28 \cdot 10^{-2}$ | $2.26 \cdot 10^{-1}$ | $-8.20 \cdot 10^{-3}$ | 1.10 |
| 200 | $4.97 \cdot 10^{-2}$ | $4.09 \cdot 10^{-1}$ | $3.97 \cdot 10^{-3}$ | 2.51 |
| 400 | $1.04 \cdot 10^{-1}$ | $3.93 \cdot 10^{-1}$ | $-6.71 \cdot 10^{-3}$ | 3.38 |
| 600 | $1.79 \cdot 10^{-1}$ | $3.02 \cdot 10^{-1}$ | $-5.38 \cdot 10^{-2}$ | 4.83 |
| $\frac{R_{200}}{3}$ | $5.35 \cdot 10^{-2}$ | $4.45 \cdot 10^{-1}$ | $8.85 \cdot 10^{-3}$ | 1.69 |

Table B.5: Fitting parameters for perturbed clusters selected by $\langle w \rangle$ parameter

| Smoothing Scale [kpc] | A_0 | A_1 | A_2 | χ^2 |
|-----------------------|----------------------|----------------------|-----------------------|----------|
| 60 | $3.43 \cdot 10^{-3}$ | $3.75 \cdot 10^{-1}$ | $3.26 \cdot 10^{-5}$ | 0.85 |
| 100 | $1.76 \cdot 10^{-2}$ | $2.76 \cdot 10^{-1}$ | $-4.83 \cdot 10^{-3}$ | 1.08 |
| 200 | $5.94 \cdot 10^{-2}$ | $3.58 \cdot 10^{-1}$ | $-1.26 \cdot 10^{-2}$ | 2.98 |
| 400 | $7.66 \cdot 10^{-2}$ | $6.14 \cdot 10^{-1}$ | $1.22 \cdot 10^{-2}$ | 2.20 |
| 600 | $5.74 \cdot 10^{-1}$ | $9.39 \cdot 10^{-2}$ | $-4.51 \cdot 10^{-1}$ | 3.20 |
| $\frac{R_{200}}{3}$ | $1.25 \cdot 10^{-1}$ | $3.16 \cdot 10^{-1}$ | $-4.17 \cdot 10^{-2}$ | 1.20 |

Table B.6: Fitting parameters for relaxed clusters selected by $\langle w \rangle$ parameter

Acknowledgments

I would like to thank first of all my parents, my sister and all my family for the support they gave me during all my academic path, supporting each choice and decision of mine.

A huge thank you goes to the supervisor of this thesis, Doctor Franco Vazza, for all that he taught me and the patience with which he followed me, providing me with knowledge and support, and transmitting the passion for the covered topics. Thanks also for letting me directly know some collaborators and giving me the opportunity to exchange opinions and ideas about this work with them.

It would be impossible to forget all friends with whom I shared this path. Thanks to the old friends, who -despite the distance- always had a minute to talk to me; thanks to the 'new' friends with whom we have shared studying moments (few) and funny ones (many). Thanks to Giacomo, Michael and Silvia and to their sofa that hosted me for months when there was the need; thanks to Attilio for sharing with me the days and the evenings between a thesis, an exam and '*na bireta*'.

Last but not least, thanks to Valentina, a everyday support, an essential person in my life and without whose help I would have never arrived where I am now.

Thanks to all those who have shared their time with me, their ideas and who have supported and held me up me during these years.

Ringraziamenti

Vorrei ringraziare in primis i miei genitori, mia sorella e tutta la mia famiglia per il supporto che mi hanno dato durante tutti gli anni dell'università, appoggiando ogni mia scelta e decisione.

Un enorme grazie va al supervisore di questa tesi dottor Franco Vazza, per tutto ciò che mi ha insegnato e la pazienza con la quale mi ha seguito, fornendomi nozioni e supporto e trasmettendomi la passione per gli argomenti trattati. Grazie anche per avermi permesso di conoscere direttamente alcuni dei suoi collaboratori e avermi dato la possibilità di scambiare con loro pareri e idee sul lavoro svolto.

Come non ringraziare tutti gli amici con i quali ho condiviso questo percorso. Agli amici di sempre, che se pur lontani, hanno sempre un minuto per scambiare due chiacchiere, ai 'nuovi' amici con i quali abbiamo condiviso momenti di studio (pochi) e divertimento (tanti). Grazie a Giacomo, Michael e Silvia e al loro divano che mi ha ospitato per mesi quando c'è stato bisogno; grazie a Attilio per aver condiviso con me le giornate e le serate tra una tesi, un esame e 'na bireta.

Per ultima ma non ultima, grazie a Valentina, sostegno di tutti i giorni, persona fondamentale della mia vita e senza il cui aiuto non sarei mai arrivato dove sono ora.

Grazie a tutti coloro che hanno condiviso con me il loro tempo, le loro idee e che mi hanno supportato e sopportato in questi anni.

List of Figures

| | | |
|-----|---|----|
| 1.1 | X-ray emission in red (XMM-Newton), radio emission at 323 MHz in blue (low resolution, beam FWHM $\sim 22'' \times 18''$) by Bonafede et al. (2014) | 4 |
| 1.2 | Original figure by Sunyaev & Zeldovich (1980). In solid line is shown the original CMB spectrum, while in dashed line is shown the spectrum after a multiple Compton scattering (i.e. the thermal SZ effect) | 5 |
| 2.1 | Energy spectrum as a function of the size of the eddies (Sinha, 2013) | 15 |
| 2.2 | Detailed view of the projected pressure distribution of the central region of the Coma cluster, presented by Schuecker et al. (2004) and observed with XMM-Newton. The 145 kpc scale corresponds to the largest size of the turbulent eddies indicated by the pressure spectrum. The smallest turbulent eddies have scales of around 20 kpc. | 25 |
| 2.3 | Spectra of FeXXV He- α from the outer region. Gaussian fits have been made to lines with energies (marked in red) from laboratory measurements in the case of He-like FeXXV, Instrumental broadening with (blue line) and without (black line) thermal broadening are indicated. The redshift is the cluster value to which the data were self-calibrated using the He- α lines. The strongest resonance (w), intercombination (x,y) and forbidden (z) lines are indicated. Spectra from paper Hitomi Collaboration et al. (2016) | 26 |
| 3.1 | Cumulative profile of kinetic, turbulence and thermal energy for cluster IT90_3 at $z = 0$, considering two different smoothing scales (60 kpc on the top and 600 kpc on the bottom) | 28 |

LIST OF FIGURES

| | | |
|------|---|----|
| 3.2 | Maps of volume-weighted mean unsmoothed velocity field (on the top- left panel), smoothed velocity field (on the top-right panel) and turbulence velocity field (on bottom panel) for the cluster IT90_3 at $z = 0$ | 29 |
| 3.3 | Map of central slice of IT90_3, turbulence velocity field without the application of shocks filter on the left panel and map of the same region with shocks filter on the right one. | 30 |
| 3.4 | All turbulence velocity profiles for shock unfiltered velocity field and shock filtered velocity filed (on the left panel) and median of the same profiles (on the right panel) | 30 |
| 3.5 | Mach number histogram of the shocks with $\mathcal{M} \geq 1.3$ in cluster IT90_3 at $z = 0$ | 32 |
| 3.6 | Map of central slice of IT90_3 at $z = 0$; map of projected Mach number (on the left panel) and map of projected flux of kinetic energy (on the right panel). | 33 |
| 4.1 | Density maps (on the top panel) and temperature maps (on the bottom panel) for all clusters used in this work (density color scale in unit of $[g\text{ cm}^{-3}]$ and temperature color scale in unit of Kelvin degrees) | 36 |
| 4.2 | Density profiles (on the left panel) and temperature profiles (on the right panel) | 37 |
| 4.3 | α radial profile for all clusters and for each smoothing scales | 40 |
| 4.4 | Median profiles for each smoothing scales | 41 |
| 4.5 | Median profiles and best fit relation for each smoothing scales | 43 |
| 4.6 | The symbols in the plot give the value of α parameter for the different smoothing scales, while the fit is obtain as described in the paragraph above | 44 |
| 4.7 | Median profiles for each smoothing scale and for high and low mass sub-samples | 46 |
| 4.8 | Less massive clusters (on the top panel) and more massive clusters (on the bottom panel) fitted for each smoothing scale | 47 |
| 4.9 | Mass- $\langle c \rangle$ relation (on the top panel) and mass- $\langle w \rangle$ relation (on the bottom panel) for each clusters | 49 |
| 4.10 | Median profiles for each smoothing scale and for perturbed and relaxed sub-samples for $\langle c \rangle$ parameter | 50 |
| 4.11 | Median profiles for each smoothing scale and for perturbed and relaxed sub-samples for $\langle c \rangle$ parameter, zoomed in the region $0 < r < 0.4R_{200}$ | 51 |

LIST OF FIGURES

| | | |
|------|---|----|
| 4.12 | Comparison between α in the core and $\langle c \rangle$ parameter for each cluster (on the top panel) and comparison between α_{200} and $\langle c \rangle$ parameter for each cluster (on the bottom panel). | 52 |
| 4.13 | Median profiles for each smoothing scale and for high and low mass sub-samples for $\langle w \rangle$ parameter | 53 |
| 4.14 | Comparison between α_{200} and $\langle w \rangle$ parameter for each cluster | 54 |
| 4.15 | Comparison between our model and the model proposed by Nelson et al. (2014) | 56 |
| 4.16 | Comparison between our α median profiles for each smoothing scale and the observed data points by Eckert et al. (2018) | 58 |
| A.1 | Schematic work-flow | 66 |

LIST OF FIGURES

List of Tables

| | | |
|-----|--|----|
| 4.1 | Catalog of clusters at $z = 0$ used in our analysis. The bold values are used to identify the perturbed clusters, based on the ranking of their $\langle c \rangle$ or $\langle w \rangle$ values, respectively. | 38 |
| 4.2 | Fitting parameters for our model | 42 |
| 4.3 | Mass sub-samples | 46 |
| 4.4 | $\langle c \rangle$ sub-samples | 48 |
| 4.5 | $\langle w \rangle$ sub-samples | 48 |
| 4.6 | Fitting parameters for Nelson model | 55 |
| B.1 | Fitting parameters for high mass sample | 68 |
| B.2 | Fitting parameters for low mass sample | 68 |
| B.3 | Fitting parameters for perturbed clusters selected by $\langle c \rangle$ parameter | 68 |
| B.4 | Fitting parameters for relaxed clusters selected by $\langle c \rangle$ parameter | 69 |
| B.5 | Fitting parameters for perturbed clusters selected by $\langle w \rangle$ parameter | 69 |
| B.6 | Fitting parameters for relaxed clusters selected by $\langle w \rangle$ parameter | 69 |

LIST OF TABLES

Bibliography

- Beresnyak A., Miniati F., 2016, *ApJ*, 817, 127
- Bonafede A., Feretti L., Murgia M., Govoni F., Giovannini G., Dallacasa D., Dolag K., Taylor G. B., 2010, *A & A*, 513, A30
- Bonafede A., Intema H. T., Brügger M., Girardi M., Nonino M., Kantharia N., van Weeren R. J., Röttgering H. J. A., 2014, *ApJ*, 785, 1
- Braginskii S. I., 1958, *Soviet Journal of Experimental and Theoretical Physics*, 6, 358
- Brighenti F., Mathews W. G., 2002, *ApJ*, 573, 542
- Brügger M., 2003, *ApJ*, 593, 700
- Bryan G. L., et al., 2014, *ApJS*, 211, 19
- Cassano R., Brunetti G., 2005, *MNRAS*, 357, 1313
- Cavaliere A., Fusco-Femiano R., 1976, *A & A*, 49, 137
- Clausius R., 1870, *De la fonction potentielle du Potentiel*
- Dolag K., Vazza F., Brunetti G., Tormen G., 2005, *MNRAS*, 364, 753
- Eckert D., et al., 2018, preprint ([arXiv:1805.00034](https://arxiv.org/abs/1805.00034))
- Ettori S., Tozzi P., Borgani S., Rosati P., 2004, *A & A*, 417, 13
- Gaspari M., Melioli C., Brighenti F., D'Ercole A., 2011, *MNRAS*, 411, 349
- Gaspari M., et al., 2018, *ApJ*, 854, 167
- Ghirardini V., Ettori S., Amodeo S., Capasso R., Sereno M., 2017, *A & A*, 604, A100
- Gitti M., Brighenti F., McNamara B., 2012, *Advances in Astronomy*, 2012, 950641

BIBLIOGRAPHY

- Hitomi Collaboration et al., 2016, *Nature*, **535**, 117
- Kaiser N., 1986, *MNRAS*, **222**, 323
- King I., 1962, *ApJ*, **67**, 471
- Kolmogorov A., 1941, *Akademiia Nauk SSSR Doklady*, **30**, 301
- Kolmogorov A. N., 1962, *Journal of Fluid Mechanics*, **13**, 82–85
- Komatsu E., et al., 2011, *ApJS*, **192**, 18
- Kraichnan R. H., 1965, *The Physics of Fluids*, **8**, 1385
- Lau E. T., Kravtsov A. V., Nagai D., 2009, *ApJ*, **705**, 1129
- Mohr J. J., Fabricant D. G., Geller M. J., 1993, *ApJ*, **413**, 492
- Nelson K., Lau E. T., Nagai D., 2014, *ApJ*, **792**, 25
- Norman M. L., Bryan G. L., 1999, in Röser H.-J., Meisenheimer K., eds, *Lecture Notes in Physics*, Berlin Springer Verlag Vol. 530, The Radio Galaxy Messier 87, p. 106 ([arXiv:astro-ph/9802335](https://arxiv.org/abs/astro-ph/9802335)), [doi:10.1007/BFb0106425](https://doi.org/10.1007/BFb0106425)
- Piffaretti R., Valdarnini R., 2008, *A & A*, **491**, 71
- Planck Collaboration et al., 2011, *A & A*, **536**, A10
- Planck Collaboration et al., 2013, *A & A*, **550**, A131
- Planelles S., Schleicher D. R. G., Bykov A. M., 2015, *Science & Space Review*, **188**, 93
- Porter D. H., Woodward P. R., 1994, *ApJS*, **93**, 309
- Porter D. H., Jones T. W., Ryu D., 2015, *ApJ*, **810**, 93
- Rajpurohit K., et al., 2018, *ApJ*, **852**, 65
- Rasia E., et al., 2006, *MNRAS*, **369**, 2013
- Roediger E., Brüggén M., 2008, *MNRAS*, **388**, L89
- Ryu D., Kang H., Cho J., Das S., 2008, *Science*, **320**, 909
- Sanders J. S., Fabian A. C., Smith R. K., 2011, *MNRAS*, **410**, 1797
- Sartoris B., et al., 2016, *MNRAS*, **459**, 1764

BIBLIOGRAPHY

- Savini F., et al., 2018, [MNRAS](#), **478**, 2234
- Schuecker P., Finoguenov A., Miniati F., Böhringer H., Briel U. G., 2004, [A & A](#), **426**, 387
- Shi X., Komatsu E., 2014, [MNRAS](#), **442**, 521
- Shore S. N., 2007, *Astrophysical Hydrodynamics: An Introduction*
- Sinha N., 2013, *Towards RANS Parameterization of Vertical Mixing by Langmuir Turbulence in Shallow Coastal Shelves*
- Spitzer L., 1962, *Physics of Fully Ionized Gases*
- Sunyaev R. A., Zeldovich Y. B., 1970, [APSS](#), **7**, 3
- Sunyaev R. A., Zeldovich I. B., 1980, [ARAA](#), **18**, 537
- Vazza F., Brunetti G., Gheller C., 2009, [MNRAS](#), **395**, 1333
- Vazza F., Brunetti G., Gheller C., Brunino R., Brügger M., 2011, [A & A](#), **529**, A17
- Vazza F., Brügger M., Gheller C., 2013, [MNRAS](#), **428**, 2366
- Vazza F., Jones T. W., Brügger M., Brunetti G., Gheller C., Porter D., Ryu D., 2017, [MNRAS](#), **464**, 210
- Vazza F., Angelinelli M., Jones T. W., Eckert D., Brügger M., Brunetti G., Gheller C., 2018, [MNRAS](#), in press
- Voigt L. M., Fabian A. C., 2006, [MNRAS](#), **368**, 518
- Wittor D., Vazza F., Brügger M., 2017, [MNRAS](#), **464**, 4448
- Zhuravleva I., Churazov E., Kravtsov A., Lau E. T., Nagai D., Sunyaev R., 2013, [MNRAS](#), **428**, 3274
- Zhuravleva I., et al., 2014, [Nature](#), **515**, 85